Doctoral Thesis

MANIPULATION OF NANOSCALE WRINKLES ON TRANSPARNET AND FLEXILBE FILMS FOR MULTI-MODAL STRUCTURL COLORATION

Jun Gyu Park

Department of Mechanical Engineering

Ulsan National Institute of Science and Technology

2023

MANIPULATION OF NANOSCALE WRINKLES ON TRANSPARNET AND FLEXILBE FILMS FOR MULTI-MODAL STRUCTURL COLORATION

Jun Gyu Park

Department of Mechanical Engineering

Ulsan National Institute of Science and Technology

MANIPULATION OF NANOSCALE WRINKLES ON TRANSPARNET AND FLEXILBE FILMS FOR MULTI-MODAL STRUCTURL COLORATION

A dissertation
submitted to the Ulsan National Institute of Science and Technology
in partial fulfillment of the
requirements for the degree of
Doctor of Philosophy

Jun Gyu Park

12. 22. 2022
Approved by

_____

Advisor
Taesung Kim

ULSAN NATIONAL INSTITUTE OF SCIENCE AND TECHNOLOGY

MANIPULATION OF NANOSCALE WRINKLES ON TRANSPARNET AND FLEXILBE FILMS FOR MULTI-MODAL STRUCTURL COLORATION

Jun Gyu Park

This certifies that the thesis/dissertation of Jun Gyu Park is approved.

12. 22. 2022

Advisor: Taesung Kim

Hoon-Eui Jeong

Im Doo Jung

Jungyul Park

Jungchul Lee

ABSTRACT

Most materials and devices with structurally switchable color features responsive to external stimuli can actively and flexibly display various colors. However, realizing covert–overt transformation behavior, especially switching between transparent and colored states, is more challenging. Current stimulus-response pattern hiding and displaying technology responds to numerous external stimuli (temperature, light, mechanical stimulation, etc.) and causes a change in dye properties and in the spacing of nanostructures. In this phase change method, it is difficult to completely hide information because patterns are easily expressed due to limited viewing angles or irregular external conditions. Therefore, there is a need for a method of controlling a transparent nanoscale surface that can completely hide information. Thus, we introduce a method of forming traditional buckling-type corrugations using bilayer-like or trilayer film. In addition, the photonic structure is fabricated using an inkjet printing method and completely laminated into the film. Moreover, in this dissertation , we study the principle of structural color in which living organisms have color by a nanostructure without pigment and the characteristics of the nanostructured photonic crystal hidden in it and design a color-changing nanostructure for single and complex structural colors. Nanoscale wrinkles are generated on the ductile top surface of various multilayered substrates by external stimuli, and their geometrical and optical features are determined by the material and structural properties of the laminated films.

First, we develop a bilayer-like laminated film with a rigid SiO2-nanoparticle (NP)-encapsulated poly(dimethylsiloxane) (PDMS) composite structure surrounded by soft PDMS as a multidimensional structural color platform. Owing to the similarity in the optical properties of PDMS and SiO2 NPs, this device is fully transparent in the normal state. However, as their mechanical strengths differ considerably, upon compressive loading, buckling-type instability arises on the surface of the laminate, leading to the generation of 1D or 2D wrinkled patterns in the form of gratings. As a result, we demonstrate an application of the device in which quick response codes are displayed or hidden as covert–overt convertible-colored patterns for optical encryption/decryption, showing their remarkable potential for anti-counterfeiting applications.

Second, we describe a thin trilayer film that can generate various wrinkles on transparent and flexible films in the presence of external mechanical bending. In particular, the wrinkle

wavelength can be controlled on a tens of nanometer scale by modulating the material properties of each layer. This active modulation plays a critical role in determining resulting structural color spectra. In other words, the wrinkles function as a diffraction grating so that the film displays bright structural colors under bending conditions. After the bending stress is released, the wrinkles disappear and the film becomes transparent again.

Lastly, we demonstrate that the material and structural patterning technique shows remarkable potential for structural coloration applications such as multimodal displays and novel barcode-based anti-counterfeiting techniques.

Table of Contents

Chapter 1. Introduction

1.1 Structure coloration in nature

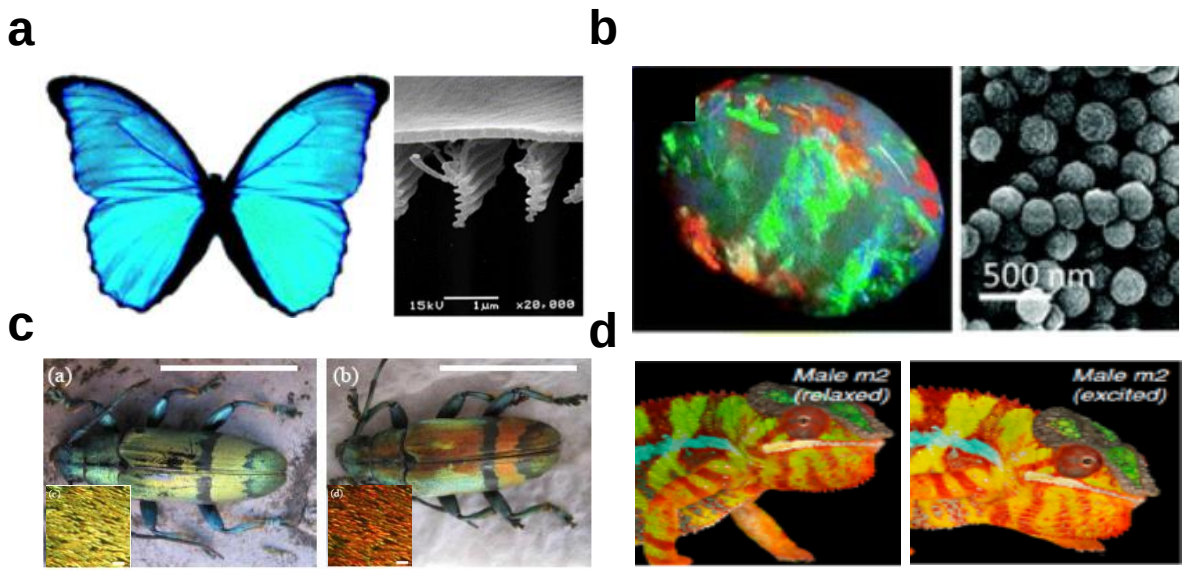

Figure 1-1. Natural photonic crystals. (a) Blue iridescence of a Morpho butterfly (left) and a scanning electron microscopy (SEM) image of its wing (right)[1]© copyright 2014 Royal Society, (b) opal gemstone (left) and SEM image of the opal structure (right)[2]© @copyright 2008 Mineralogical Society of America, (c) Longhorn beetle[3]© copyright Optica (d)Chamelon[4]© copyright 2016

Morpho butterflies have distinctive deep-blue wings. The distinctive deep blue is formed by the micro/nano surface of their wings, as shown in Figure 1-1a. The micro/nano structures distributed on the surface widely scatter light of a certain wavelength, giving the wings of the Morpho butterfly a glimmer compared to conventional natural dye pigments[1]. Opal photonic crystals composed of various lattice structures are formed along different lattice directions for each region and possess a complex structural color pattern with different structural colors according to regions. Even if the opal photonic crystal has the same lattice structure, it is consistent with the characteristic that the structural color changes because of the lattice direction that varies depending on the viewing angle[2]. Furthermore, there are organisms in

nature that change color according to the external environment to protect themselves from or alert them regarding external threats from natural enemies. These organisms have flexible viscoelastic layers that adjust the spacing of the repeated lattice by expanding or contracting under external stimuli, such as humidity[3] and stress[5,4]. As shown in Figure 1-1c, the wings of the organism in question display a color change in response to humidity. In dry conditions, the wings are green, while in wet conditions they turn red. This phenomenon occurs owing to the expansion of the multilayer flexible plate structure in the wing under increased humidity, which leads to a change in the reflected wavelengths. Finally, Figure 1-1d shows that the surface of the lizard exhibits structural colors due to the arrangement of pigment structures on the surface. These structures scatter light at different wavelengths, resulting in the colorful appearance. A regularly formed nanolattice structure occurs through the reflection or diffraction of a specific color upon interference with light, which is called a photonic crystal. To understand the diffracted light of the geometric shape and periodic characteristics of the photonic crystal structure, the macroscopic behavior of electromagnetic waves is explained using the Maxwell equation given by Equation (1-1):

$$\nabla \cdot \mathrm{B} = 0, \nabla \times \mathrm{E} + \frac{\partial B}{c\partial t} = 0 \quad .$$

(1-1)

By substituting the boundary conditions of the given structure into the Maxwell equation, the solution can be obtained through complex numerical analysis and the development of a formula. By calculating the obtained frequency as a function of the wave vector in the propagation direction, the optical band gap expected in the one-dimensional (1D) and two-dimensional (2D) photonic crystal structures can be easily identified using Bragg's law. The expected photonic bandgap in the 1D and 2D photonic crystal structures can be easily confirmed using Bragg's law given by Equation (1-2) established according to the principle of Figure 1-2[6]. In Equation

(1-2), λ is the wavelength of the expected photonic bandgap region, D is the period of the material to be arranged, n_{eff} is the average reflectance of the material used for the pore and medium, and sinθ is the angle at which light is incident on the photonic crystal structure:

$$\lambda = 2Dn_{eff}\sin\theta. \quad (1\text{-}2)$$

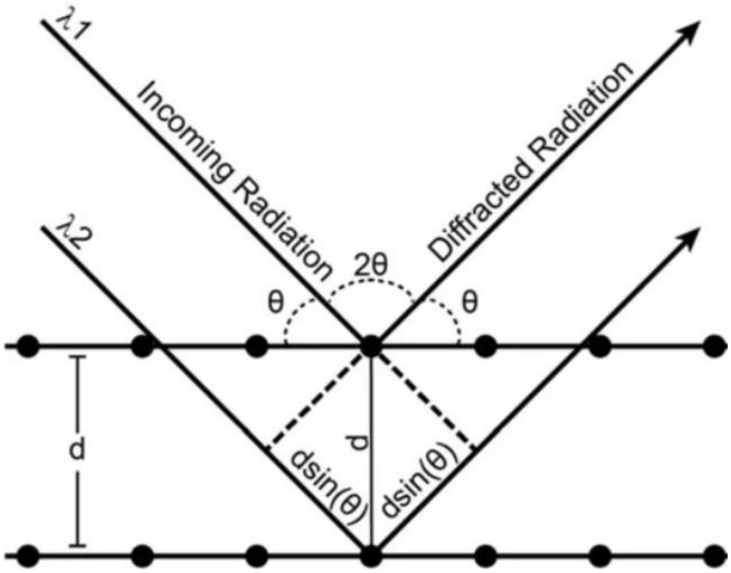

Figure 1-2. Schematic representation of Bragg's law conditions[6]. @copyright 2020, ISSN.

According to Bragg's law, the scattering of a wave off a periodic structure is characterized by a specific wavelength and angle of scattering, known as the Bragg angle. In photonic crystals, the Bragg angle is determined by the spacing between the micro/nanostructures within the crystal. The optical properties of the photonic crystal, such as the bandgap, can be modified by altering the spacing between the nanoparticles. Carefully controlling the spacing of the nanoparticles in a photonic crystal enables tuning of the optical properties of the material and creating a specific range of wavelengths that are allowed to pass through the crystal. The recent development of nanoprocessing technology has facilitated imitation of various nanostructures in nature, and this photonic crystal technology shows excellent performance in adjustment of

light using a periodic structure. The optical properties of a photonic crystal are determined by the spacing between the nanoparticles and the shape of the nanostructure. By carefully designing the spacing and shape of the nanostructure, creating photonic crystals with specific optical properties, such as a specific bandgap or a specific range of wavelengths that are allowed to pass or reflect through the material, is possible. The initial results of photonic crystal research have revealed that the optical band gap, which periodically changes the wavelength of light and does not transmit specific wavelengths in a frequency band without an external power source, is expected to revolutionize optoelectronics and optoelectronic devices[7]. This unique characteristic can simplify the manufacturing process and guide light of different wavelengths without loss of power in applications such as laser, organic light-emitting diodes (OLEDs), and photonic circuits. However, in recent years, attention has turned to the use of photonic crystals in displays and sensors that exploit their ability to change structural colors. These photonic crystals, which are close to being utilized in practical applications, have the potential to be widely applied in fields such as diagnostic medicine[8],environmental monitoring[9], and sensors[10]. They can also be produced at a relatively low cost and in large quantities, as they can be observed directly with the naked eye and do not require expensive or complex detectors when external stimuli are applied. Thus, commercialization and practicalization based on mass production are expected to be possible.

1.2 Photonic Crystal/Buckling/Wrinkle-based Nanoscale Structures

In this chapter, micro/nanoscale structural color devices, which are controlled, repeated crystal structures, are introduced. First, we classify photonic crystals according to their production method: top-down or bottom-up approach. Then we describe their responsiveness to stimuli and describe how patterned photonic crystals can be used in a variety of application structures.

Top-down fabrication

Top-down methods involve patterning using traditional lithography techniques such as photolithography, electron beam (e-beam) lithography, and focused ion beam (FIB) milling. These techniques allow precise patterning of materials at the microscale and nanoscale, enabling the creation of ordered structures with well-defined periodicity. Early attempts to fabricate structured photonic crystal patterns involved an FIB to directly etch the bulk material by removing targeted positions using an ion beam. Accordingly, complicated patterns are generated by the FIB method as shown in Figure 1-3a[11]. However, the FIB method highly relies on expensive equipment for precise control of the ion beam and has a low throughput due to the step-by-step process of directly removing the material. To overcome the problem of low throughput, e-beam etching methods have been investigated. E-beam etching is a highly precise and selective method, facilitating the creation of submicron and nanoscale features with good control over the etch depth.

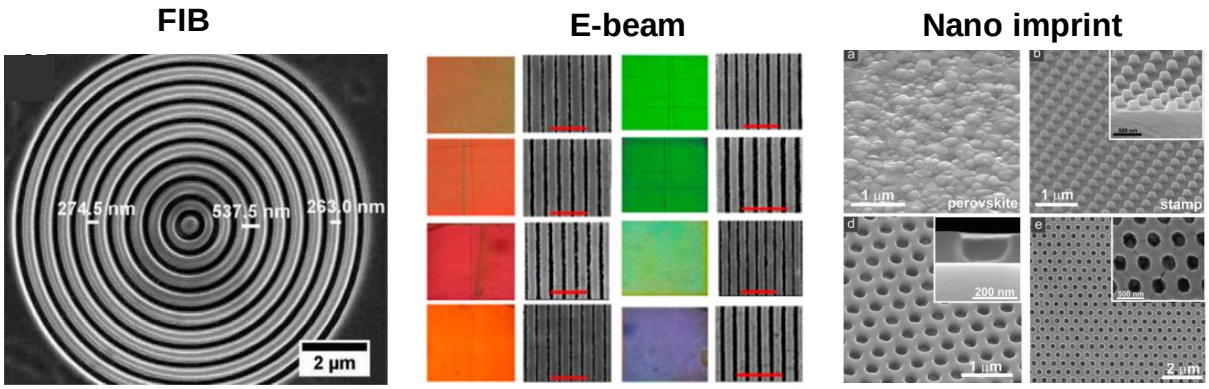

Figure 1-3. Top down method for photonic crystal fabrication. (a) FIB[11] © Copyright 2015, American Vacuum Society, (b) e-beam[12] © Copyright 2018, American Chemical Society, and (c) nanoimprint[13]© Copyright 2016, American Chemical Society.

One advantage of e-beam etching over FIB methods is its ability to pattern high-aspect-ratio structures and deep trenches with good vertical shape control in a single step. Gas-assisted etching of thin $MAPBI_3$ films generated a nano-slit array of periodic lines with submicron periodic line patterns, resulting in nano-gratings as shown in Figure 1-3[12]. Nanoimprinting is widely used for fabrication of micro-nanoscale patterns. A substrate film is first cast onto a substrate and then brought into contact with a topographically prepatterned mold and pressed at a temperature above the glass transition or softening temperature. Thus, nanoimprint lithography has been successfully demonstrated for high-throughput fabrication of photonic structures[13].

Bottom-up fabrication

The building blocks of photonic crystals are nanoparticles. The optical properties of a photonic crystal are determined by the spacing between the nanoparticles and their shape. By carefully designing the spacing and shape of the nanoparticles, creating photonic crystal structures with specific optical properties is possible. The dip coating method represents a simple process for producing photonic crystals by immersing a specific substrate in a colloidal dispersion and coating the substrate with it while moving it at a constant speed. This method relies on the formation of a surface between the substrate and the dispersion, with colloidal particles dispersed on the surface owing to the meniscus phenomenon. When the substrate is moved at a constant speed, the surface and particles will adhere to the substrate and move together, forming a film-like photonic crystal as the solvent gradually evaporates from the surface[14]. (Figure1-4a) The blading method involves placing a spacer with fine patterns of a specific thickness between the spacer and bottom substrates, allowing the solvent to escape.

When a colloidal dispersion is injected through the top substrate, colloidal particles are deposited on the bottom substrate depending on the meniscus between the spacer and bottom substrate. Accordingly, photonic crystals are formed through the fine patterns of the spacer as the solvent evaporates, as shown in Figure 1-4b. The spin-coating method can be used to fabricate a photonic crystal film on a wafer by dispersing uniform colloidal particles on a substrate and applying spin coating. This method enables the production of a photonic crystal structure with a uniform film structure over the entire wafer by controlling the thickness of the colloidal crystal through the spin speed[15]. (Figure 1-4c) However, the properties of the resulting photonic crystal may differ with periodicity depending on the substrate size. Further, the inkjet-printing method is a useful technique for the fabrication of photonic crystals owing to its ability to produce high-resolution and fine-shaped patterns, potential for noncontact printing, and compatibility with a variety of inks. This method is generally cost-effective and suitable for mass production because it does not require expensive equipment or specialized processing steps. In addition, the inkjet-printing method facilitates the fabrication control of various patterns through self-assembly control of building blocks, which can be achieved by manipulating the evaporation process of ink[16]. (Figure 1-4d)

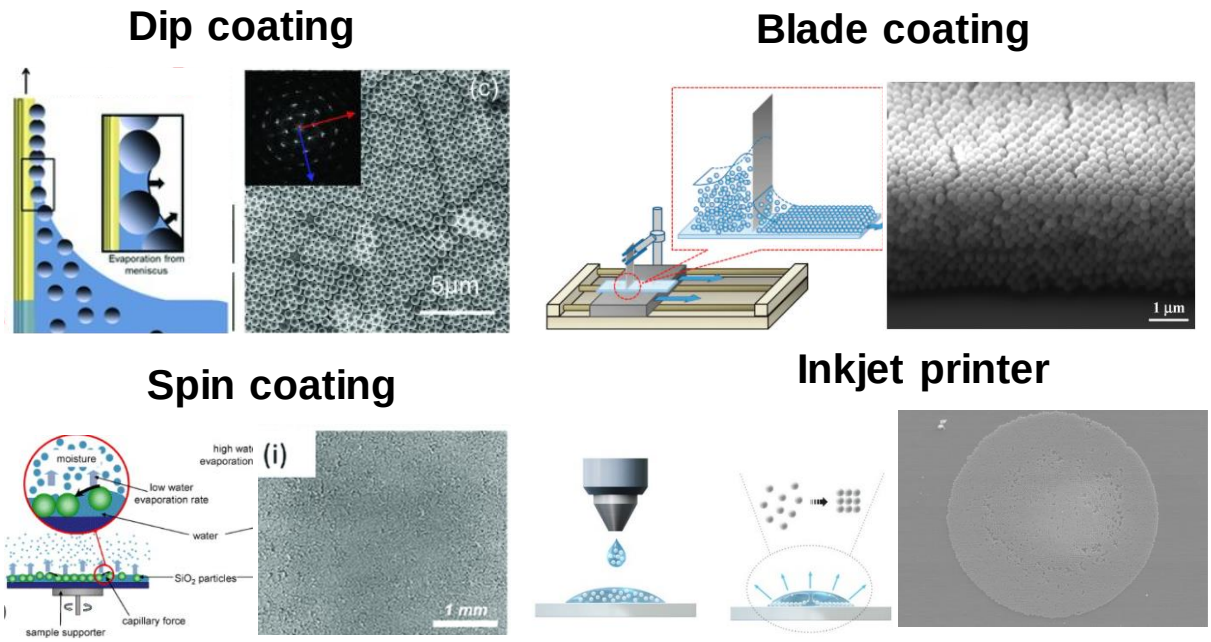

Figure 1-4. Bottom up method for photonic crystal (a) Dip coating[14]© copyright 2014 Wiley-VCH, (b) blade coating[15]© 2010 American Chemical Society, (c) spin coating[17]© copyright 2007 Elsevier, and (d) inkjet printing[16]© copyright 2016 Nature portfolio.

Stimulus-responsive structural coloration

There have been numerous efforts to create photonic crystals with a stimulus-responsive structure, allowing their use in various applications. These stimulus-responsive structure colorations can be classified into three categories according to their working mechanism.

First, reactive building blocks are directly used to build photonic crystals, and the strategy is to prepare reactive materials in the form of building blocks themselves. For example, the core–shell method involves the synthesis of nanoparticles with a core made of a material with a certain optical property and a shell made of a material with a different optical property. By controlling the material property and refractive index of the shell, the self-assembled core–shell structure shows reactivity to multiple stimuli. This method has been used to create structured color in thin films by dispersing nanoparticles in a polymer matrix and subsequently patterning the film using techniques such as lithography or self-assembly. The resulting film exhibits

structural color due to the periodic arrangement of the nanoparticles, which causes interference of the light scattered by the nanoparticles. The color of the film can be easily changed by varying the spacing between the core and shell by applying an external electric field[18] (Figure 1-5a). The other approach for fabricating structural colors involves the use of block copolymers. Designing and synthesizing block copolymers with specific physical and chemical properties enables the creation of self-assembled structures with desired photonic properties. This approach has the advantage of being able to create complex, hierarchical structures with high precision and reproducibility[19] (Figure 1-5b). However, one potential drawback of this method is the requirement of specialized equipment and the limitation of wafer-scale products.

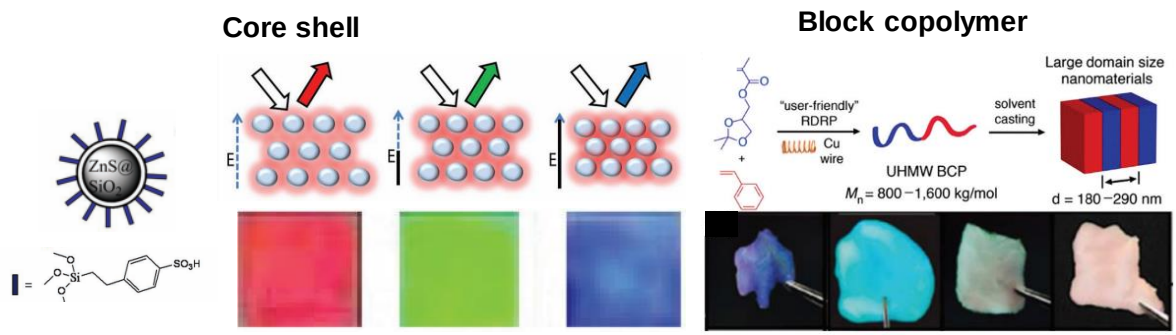

Figure 1-5. Stimulus responsive materials consists of reactive building blocks. (a) core–shell structure and self-assembled core-shell film[18]© Copyright 2012, Wiley-VCH and (b) molecularly adjusted block copolymer[19]© copyright 2016, American Chemical Society.

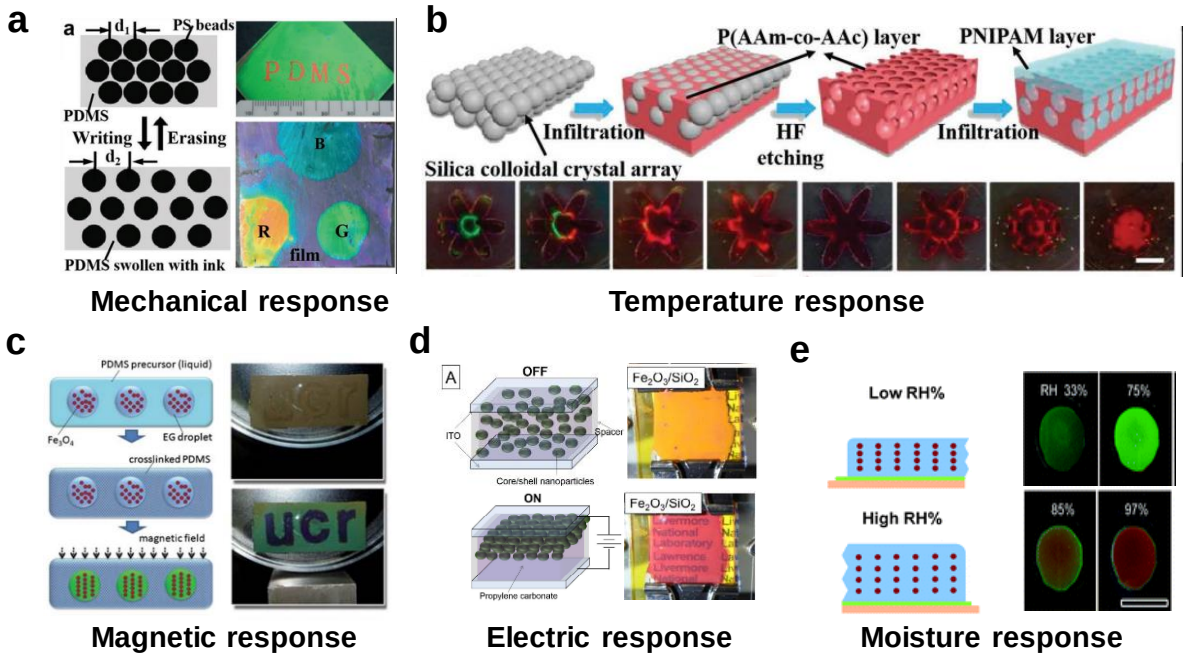

Figure 1-6. Different types of actuation responses by incorporating with response materials. (a) Chemical response[20]© Copyright 2003, Wiley-VCH, (b) temperature response[21]© Copyright 2019, Wiley-VCH, (c) magnetic response[22]© Copyright 2010, The Royal Society of Chemistry, (d) electrical response[23]© Copyright 2018, American Chemical Society, and (e) moisture response[24]© copyright 2011 Royal Society of Chemistry.

Second, incorporating responsive materials into the interstitial space of a periodic photonic crystal structure is a common method for creating stimulus-responsive structural color materials. The periodic photonic crystal structure is typically created by arranging a large number of identical nanostructures in regular, repeated patterns. Incorporating responsive materials into the interstitial space enables the fabrication of an optically tunable composite material that can change its structural color expression. These intricate structures can be used in various ways to drive actuation by utilizing the photonic crystal itself as the actuating element or as a sensing element to change color. Figure 1-6a illustrates the embedding of polystyrene colloidal arrays in an elastic polydimethylsiloxane (PDMS) matrix. A silicone fluid causes PDMS to swell and increases the lattice spacing of the colloidal arrays when applied to a composite film. Figure 1-6b describes the preparation of an inverse opal scaffold by

integrating two different types of hydrogel (poly(N-isopropyl acrylamide) (PNIPAM) and poly(acrylic acid-co-acrylamide)) layers. The thermal responses of these layers are opposite, leading to opposite volume changes and interior water circulation during heating or cooling. As the ambient temperature increases, the P(AAm-co-AAc) layer swells, causing the structure to bend toward the PNIPAM side, shifting the structural color from green to red. Further, Figure 1-6c describes a method for displaying and hiding encrypted patterns by immersing them in water. The differences in swelling rate and volume expansion between the pattern area and background result in differences in lattice constants, causing the diffracted wavelengths to have a wide range between the pattern area and background. Next, Figure 1-6d describes a method for creating a diffraction color by encapsulating an ethylene glycol solution containing Fe_3O_4@SiO_2 colloids in a PDMS matrix in the form of microdroplets. The composite PDMS film is naturally brown; however, under the application of a magnetic field, the superparamagnetic colloids in the glycol solution promptly assemble into 1D photonic crystal structures along the magnetic field lines, rapidly converting the brown color into a brilliant diffraction of colors. Third, modifying the shape of the nanostructure can result in a change in the structural color of the material. This can be achieved by transforming the shape or size of the polymeric structure, which can result in a noncolor-to-color or color-to-color change. This unique property of structural color materials makes them highly tunable and enables a wide range of color changes. For examples, shape memory polymers can undergo a reversible phase transition between a temporary shape and their permanent shape (Figure 1-7a). When stress is applied on such a material, it becomes pliable and can be deformed into a temporary shape to change periodicity. As a result, diffraction of light only occurs in the permanent shape[25]. Figure 1-7b illustrates the adhesion instability of photonic crystal structures and composite materials. When tensile stress is applied, the deformation of the composite material increases, creating a

gap between the structure and the material. This results in a color expression due to the uniformity of the gaps[26]. Another method for generating nanostructures is by inducing wrinkles on the film surface according to the buckling theory. This method uses plasma treatment to selectively harden the surface of a material. The benefit of this method is the ability to selectively harden the surface of the material to create a bilayer with different mechanical properties. This can aid in creating a nanostructure under mechanical stress[27].(Figure 1-7c)

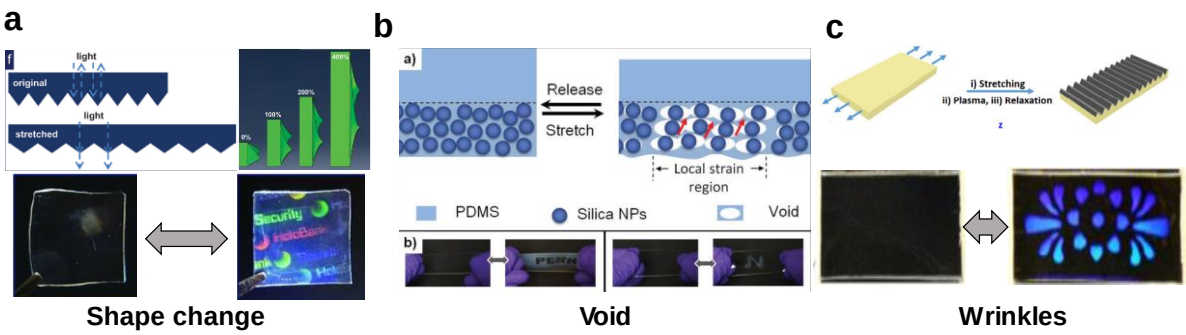

Figure 1-7. Transformation of nanostructures. (a) shape change [25]© copyright 2013 Wiley-VCH, (b) voids[26]© copyright 2015 Wiley-VCH, and (c) wrinkles [27] © copyright 2020 Springer Science

1.3 Applications of Structural Color Devices

The ability of structural color materials to change color is a result of their unique optical properties, which are determined by the periodic arrangement of nanostructures achieved by carefully designing and fabricating the photonic crystal structure. The ability to change the color of a photonic crystal has significant implications for various applications, including displays, sensors, and anti-counterfeit. In this section, recent applications are introduced and described with respect to structural coloration.

Display Photonic crystals have been explored for use in display technology, including the development of highly efficient, low-power consumption, unique displays. In display applications, photonic crystals can be used as light-emitting elements or as photonic filters. One way in which photonic crystals are used in display technology is as light-emitting elements in OLED displays. The use of photonic crystals in OLED displays can enhance the efficiency and stability of the OLEDs by confining and guiding the light emitted by the OLEDs. This is due to the unique optical properties of photonic crystals, which enable the manipulation of light at the nanoscale. The incorporation of photonic crystals into OLED displays can lead to improved performance, such as increased brightness and longer lifetimes for the OLEDs[28]. (Figure 1-8a) Structural color materials represent a promising alternative to traditional optical displays, which rely on active light-emitting elements to produce color images. Figure 1-8c shows smart, energy-efficient, and tunable structural-color films developed for use in nighttime traffic safety and advertisement displays. These films were fabricated by embedding a monolayer of polymer microspheres on the sticky side of transparent tape, forming an interferometric structure on the surface of air-cushioned microspheres. The resulting structural colors were noniridescent under coaxial illumination

and viewing conditions but appeared iridescent under noncoaxial illumination and viewing conditions[29]. Figure 1-8c depicts a low-loss dielectric metasurface-enabled brightness-tunable full-color nanopainting, which uses a periodic arrangement of TiO_2 nanopillars supported on a SiO_2 substrate with varying dimensions and orientations to produce different hues and brightness levels. The resulting nanoprinted image has a photorealistic color presentation and a stereoscopic impression[30].

Figure 1-10. Structure coloration for display application. (a)OLED 28© copyright American Chemical Society (b) Nighttime traffic safety[29] © copyright 2020, American Association for the Advancement of Science, (b) surface oxidation, and (c) photonic coating[30]© copyright 2020 Optica.

Wearable devices Photonic crystals have shown great potential for use in wearable sensors owing to their unique optical properties, which facilitate the detection of various parameters such as temperature, pressure, and humidity. These sensors operate by measuring the changes in optical response of the photonic crystal that occur in response to changes. A primary advantage of using photonic crystals in wearable sensors is their high sensitivity and accuracy. This is because photonic crystals have a highly structured and periodic arrangement, which leads to strong interaction with light and a highly sensitive response to small changes of human motion.(Figure 1-9a) structure coloration can be used as a coating for wearable sensors to improve performance due to their flexibility. For example, a photonic crystal coating could be applied to a wearable pressure sensor to monitoring the eye's pressure. This is because photonic crystal coatings have excellent mechanical and chemical stability, as well as high resistance to wear and degradation. In addition, photonic crystals can be easily integrated into various types of flexible and stretchable materials, making them well suited for use in a wide range of wearable sensor applications. (Figure 1-9b)

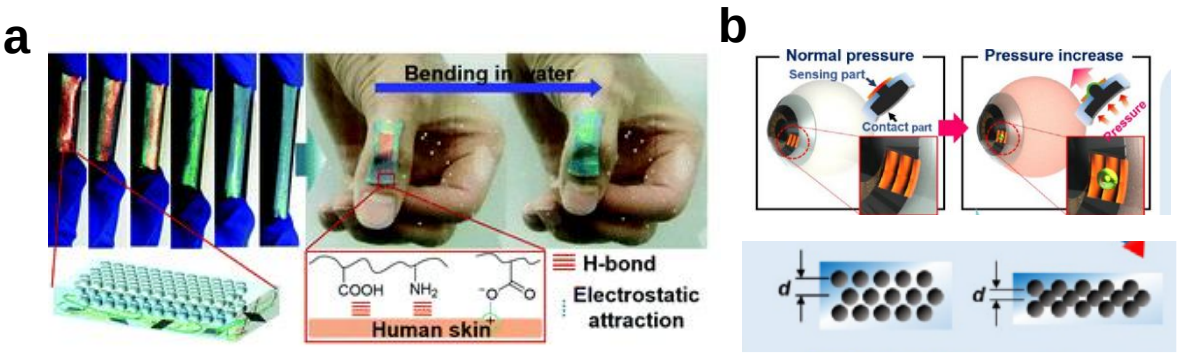

Figure 1-9. Structure coloration for wearable device (a) bilayer buckling[31]© copyright 2022, Royal Society of Chemistry and (b) surface oxidation[32]© copyright 2022, Royal Society of Chemistry.

Biosensors Structural coloration has also been explored for use in biosensors, which are sensors that are used to detect and measure various biological parameters such as pH[33], protein[34], glucose[35] and virus[36]. The stimulus responsiveness of structural color materials has made them promising sensing elements in biosensors owing to their ability to detect small changes in their surrounding environment. Photonic crystal-based biosensors offer many advantages over other microfluidic and nanotechnology-based biosensing applications, including cost-effective manufacturing and shorter assay times. For example, photonic crystals can be used to detect by measuring the shifts in their optical properties that occur in response to changes in the of their environment. A primary advantage of using photonic crystals in biosensors is their high sensitivity and accuracy. Additionally, photonic crystals can be easily integrated into various types of biosensors, including those that are portable and wearable, making them well suited for use in a wide range of biosensing applications. For example, a photonic crystal-based glucose sensor could be integrated into a wearable device for continuous monitoring of blood glucose levels in people with diabetes.

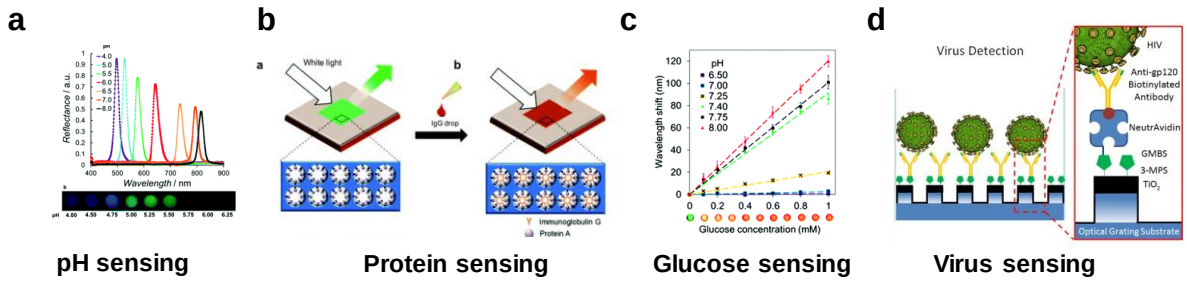

Figure 1-11. Structure coloration for biosensor application. (a) pH sensing[33]© copyright 2014 , Wiley-VCH (b) protein sensing[34]© copyright Elsevier, (c) glucose sensing[35]© American Chemical Society, and (d) virus sensing[36]© Nature portfolio

Anti-counterfeiting Structural color materials have tunable colors and visual effects in response to various external stimuli, which make them difficult to imitate. Because structure coloration is produced by the physical properties of a material rather than pigments, it is difficult for counterfeiters to imitate the dynamic functionalities and encryption-decryption strategies of structure coloration. They are considered more secure than traditional anti-counterfeiting materials such as holograms, concave–convex patterns, watermarks, and fluorescent ink, which are widely used in security documents, packaging, and brand protection[37]. The purpose of structure coloration in anti-counterfeiting applications focused on complexity, functionality such as 4D Pattern, color barcode and color encoding system. As shown in figure 1-8a The PVDF BLIHS film which have paradoxical features of ordered and quasi-amorphous arrays. Complex patterns could be encryption by surrounding feature and only decryption by smart phone[38]. Figure 1-8b shows the three kinds of pattern integrated sequentially into one pattern using the layer-by-layer printing strategy by controlling the rheology of PDMS. As a result different message are encoded in one film[39]. Figure 1-8c shows a method for protecting hidden messages using three different defense strategies: characteristic optical stopbands, algorithm encryption and angle-dependent encryption[40].

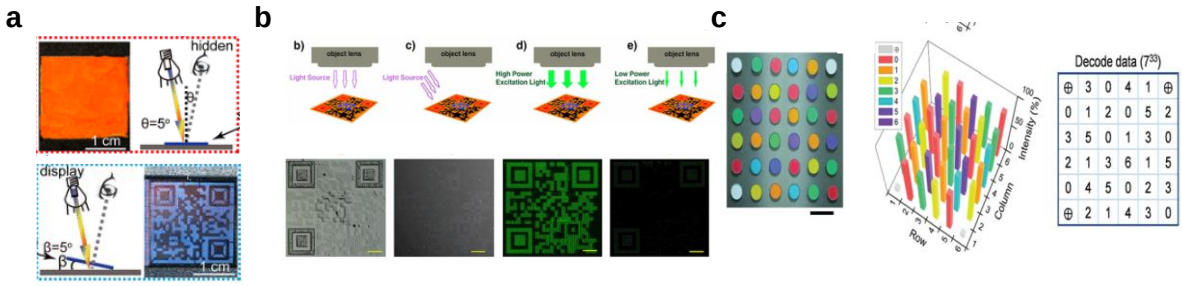

Figure 1-12. Structure coloration for anti-counterfeit application (a) angle dependent pattern[38]© copyright 2017, Royal Society of Chemistry, (c) 4D pattern[39]© copyright Wiley-VCH, and (c) color encoding system[40]© copyright 2017,Royal Society of Chemistry

Although significant progress has been made in the development of structure coloration-based application. First, additional research on the stability and durability of structure coloration materials is necessary to realize their full potential as various application. Second, most demonstrations of structure coloration-based technologies are at a small scale, and realizing a repeatable mass-production process for these materials with consistent periodic structure and uniform response properties remains a significant challenge. Finally, controlling the uniform discoloration of photonic crystal in their transparent state is an ongoing area of research. The development of transparent stimulus response materials with multiple stimulus-response capabilities holds great promise for the creation of advanced anti-counterfeiting systems. Further research in this area will possibly lead to various new optical structure coloration technologies.

Chapter2 Bilayer-like Film

2.1 Introduction

In nature, some animals change their colors upon stimulation to hide from enemies and predators or to communicate with their rivals or mates. Most of these properties are based on stimulus-responsive structurally switchable colors as a result of changes in the micro-/nanostructure of the surface in response to external stimuli. Inspired by these phenomena, a variety of materials have been developed that undergo color changes flexibly according to external stimuli such as mechanical force,[41,42] biomechanical actuation,[43,44] temperature,[45] a chemical component,[46] electrical force,[47] or magnetic force.[48] Specific responsive performance of this nature means that structural coloration techniques are potentially highly suitable for use in sensors,[49, 50] robots,[51] smart windows,[52] and anti-counterfeiting applications.[53] In particular, the ability to rapidly and repeatedly switch colors as a result of structural changes under the influence of external stimuli has attracted considerable attention because of the technical convenience and practical applicability of these characteristics in security markets.

However, to date, most materials with structural coloration properties and devices that respond to external stimuli are known to be able to undergo transformation between two or more different colors. Therefore, it seems still challenging and attractive to develop materials and devices with the ability to transform between transparent and colored states. For example, optically transparent elastomeric shape memory polymers were used to fabricate a coloration device that can switch between as-fabricated and programmed (or temporarily deformed) configurations.[25, 54] As a result, the device showed a transformable ability to switch between transparent and colored states. In addition, a digital control method for local stresses in shape memory polymer materials was developed to freely manipulate the refractive index of transparent materials in various directions.[55] This leads to a two-dimensional (2-D) film that

is invisible under regular light but can be visualized under polarized light due to the birefringence. It is true that these studies showed irreplaceable advantages such as rewritability. However, it is also true that such materials require complicate processes for color generation or their manipulation mechanisms are complex for geometrical restoration. Therefore, it still remains a challenge to either realize available artificial materials with the ability to structurally switch colors or develop coloration devices responding to external stimuli in a simple and controllable manner to display colors. The ability to exhibit covert–overt transformation can be additionally beneficial to anti-counterfeit applications of structural coloration materials/devices. In this paper, we present a device based on transparent, flexible, and covert–overt structural conversion that utilizes the similar refractive indices and considerably different mechanical strengths of poly(dimethylsiloxane) (PDMS) and SiO_2 nanoparticles (NPs). We developed a simple process to fabricate the SiO_2-NP-encapsulated PDMS device and then characterized the wrinkle arrays generated at the surface under compressive bending stress. We further investigated the multi-dimensional structural coloration mechanism, which depends on the viewing angle, and in which the wrinkle arrays act as transmission/diffraction gratings. We also demonstrated the applicability of such a device to covert–overt anti-counterfeiting techniques using images that are easily transformed by mechanical stimuli; for example, two quick response (QR) codes are patterned on the two sides of the device and then their structural colors are displayed by finger-loaded compressive stresses on demand, thereby demonstrating a practical, simple, convenient, and highly secure anti-counterfeiting application.

2.2Material and method

Material printer: The pattern of self-assembled NP structures on the substrates was prepared using a piezoelectric drop-on-demand inkjet printer (DMP-2800, Fujifilm Dimatix, Inc., CA, USA) with a cartridge (Model No. DMC-11610).[56, 57] It consisted of 16 independent operational nozzles in one row with a spacing of 254 μm and diameter of approximately 21.5 μm. Each nozzle can support droplets of 10 pL. The center-to-center droplet spacing can be controlled from 5 μm to 254 μm by adjusting the angle of the printer head in 1-μm increments, depending on the resolution setting (9 dpi). A droplet spacing of 150 μm was maintained throughout the entire fabrication process to prevent overlapping of droplets.

Reagents and materials: The ink was prepared by centrifuging 1 mL of a solution of mono-dispersed silica NPs (20% w/v) with a diameter of 500 nm (Polysciences, Warrington, USA) at 4000 rpm for 12 min, and then the clear solution was discarded. The remaining pellet containing the NPs was collected and mixed with formamide (Sigma Aldrich, Korea) to obtain a NP suspension of 20%. The mixed NP suspension as prepared was ultra-sonicated for 20 min to ensure complete dispersion (5510E-DTH, Bransonic, USA) and was used as the ink solution. The preparation procedure was the same for solutions of 300 nm as well as 700 nm particles (Polysciences, Warrington, USA). Surface wrinkles on compressed structural color platform were replicated by using PUA (MINS-311RM, Minuta Tech., Osan, Korea).

Printing conditions: Different SiO_2-NP patterns can be achieved by inkjet printing the SiO_2 suspension (20% w/v) on glass substrates with different wettability at various temperatures.[58] Printing of monolayer structure: to print a SiO_2-NP self-assembled monolayer structure, the glass surface was first treated by piranha cleaning to increase the wettability (contact angle, CA = 10°). Then inkjet printing was implemented with a substrate temperature of 28 ℃. Printing of coffee-ring patterns: coffee-ring patterns were obtained by using inkjet printing on

pristine glass (CA = 17°) with a substrate temperature of 38 ℃, resulting in a much easier to generate flow of Marangoni at the edge of the water droplet. Printing of dome structures: dome structures were printed on chlorotrimethylsilane-treated glass (CA = 90°) with a substrate temperature of 28 ℃. After the printing and self-assembly of NPs were complete, all the samples were dried at 90 ℃ for 30 min to ensure the complete volatilization of formamide.

PDMS transferring: A PDMS mortar with base to curing agent in a 10:1 mixing ratio was degassed for 30 min in vacuum to remove the air bubbles. Then, the PDMS mortar was poured on the prepared pattern of self-assembled NP structures on the glass substrate and kept in an oven for 12 h at 75 ℃. The cured PDMS was subsequently removed from the oven and allowed to cool for 30 min. Then, the pattern of nanostructures on the glass was transferred and encapsulated in the PDMS matrix.[45]

Characterization: All the CAs reported in this study were measured by a goniometer (Smart Drops SDL200TEZD, Femtofab Co. Ltd., Pohang, Korea). A droplet of deionized water (1 μL) was gently placed onto the glass substrates of which the wettability differed as a result of treatment of the surface of a SMART drop using various chemical processes. The averaged value of the CA reported is the mean of 10 measurements of the CA. SEM images were captured and utilized to study the morphology and spatial distribution of the resulting silica nanostructures/deposits (S-4800, Hitachi, Japan). Two types of CCD cameras were used: an SLR CCD camera (Nikon D300, Nikon, Japan) for high-quality images and an iPhone 6S for regular images. The spectra were recorded using a UV–visible–NIR microspectrophotometer (20/20 PV UV−visible−NIR microspectrophotometer, Craic Technologies, San Dimas, CA, USA). A mobile phone, a Samsung Galaxy Note9 (SM-N960N) and commercial AAP Official QR code Reader “Q” (DENSO Co., Japan), Logo QR barcode scanner (Funcode technology) were used for QR code recognition.

2.3 Result and discussion

Figure 2-1 shows the fabrication process of the SiO_2-NP-encapsulated PDMS device. A colorful image is first converted into a monochromic bitmap; then, ink droplets containing SiO_2-NPs are injected only on the black dots at 150 μm intervals. Each injected droplet evaporates and forms a coffee-ring-shaped nanostructure on the glass substrate. Then, we pour PDMS mortar into these nanostructures to encapsulate the SiO_2-NP patterns, followed by curing, after which the PDMS slab is peeled off as illustrated in Figure 1a and also in Figure S1a. We chose coffee-ring-shaped nanostructures after testing several shapes, as described later. Figure 1b shows the coffee-ring pattern on the glass substrate before PDMS encapsulation. The glass substrate with the pattern is indicated with a dashed-line rectangle in green, and a white "UNiST" logo is shown against a black background. In this case, no color can be seen clearly, but the glass appears slightly white because of the light interference with the irregular nanoparticle arrangement, as demonstrated in our previous work.[16] The enlarged scanning electron microscopy (SEM) images clearly show that each bitmap pixel is reconfigured with self-assembled SiO_2-NP nanostructures. The additionally magnified SEM image shows a single coffee-ring-shaped nanostructure, in which the center is empty but surrounded with NPs. It resembles a half-cut donut with a relatively higher aspect ratio than typical coffee-ring structures, facilitating deeper and more effective permeation of PDMS.

Figure 2-1c shows a completed SiO_2-NP-encapsulated PDMS device in which the same pattern as in Figure 2-1b was transferred and placed on the same background as indicated with a dashed-line rectangle in green. PDMS was chosen to encapsulate the SiO_2-NP-based nanostructure pattern because it has a very similar refractive index (i.e., n_{SiO_2} = 1.475 and n_{PDMS}= 1.43).[58, 59]

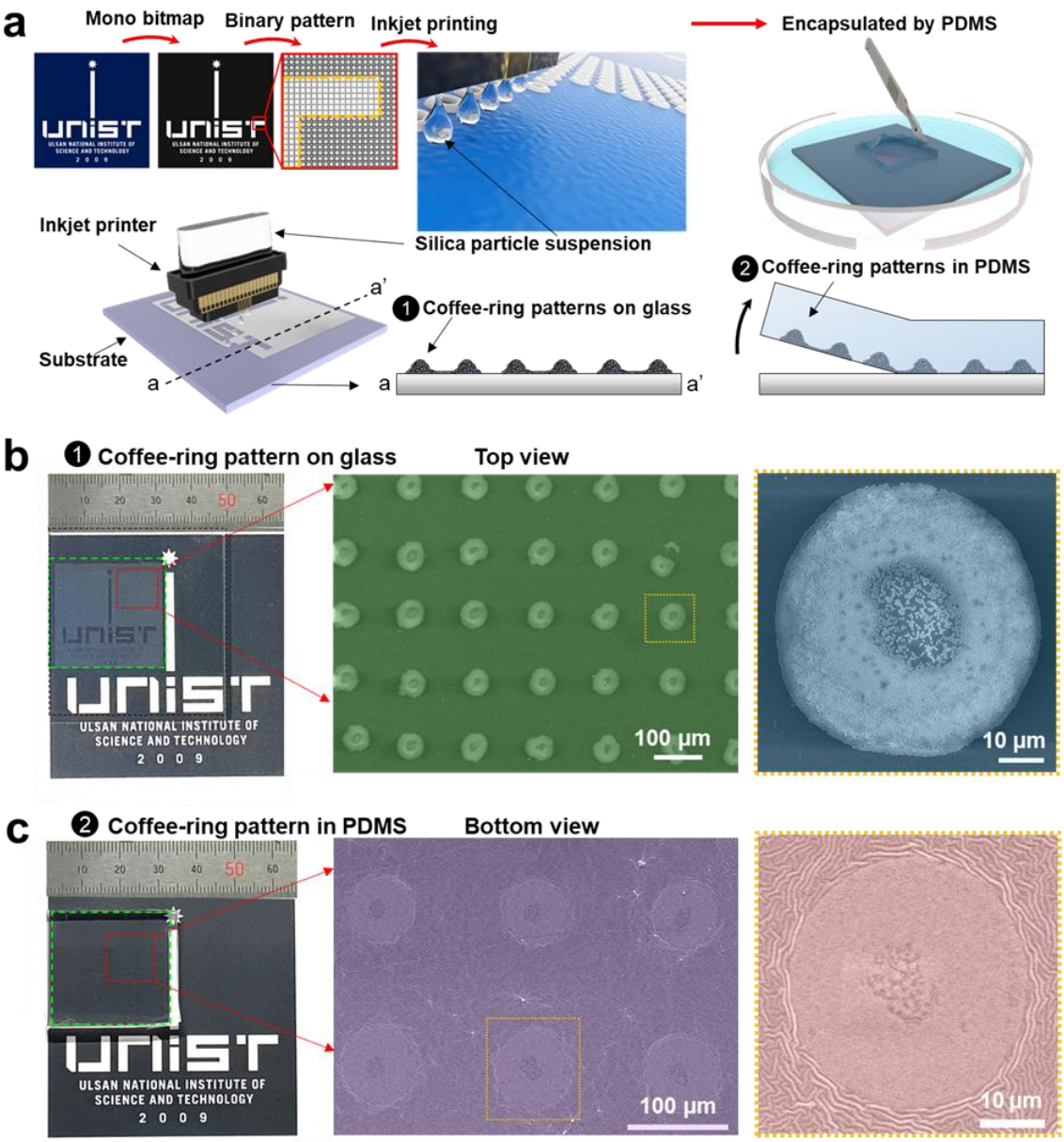

Figure 2-1. Concept and fabrication process. (a) Schematic showing the conversion of a color image to a black-and-white bitmap to generate droplet-based binary patterns for inkjet printing and subsequent transfer by PDMS. (b) Optical image of the glass after inkjet printing on a black background. On the right are SEM images of the coffee-ring-shaped nanostructure patterns produced by injecting the SiO_2 NP suspension on the glass slide. (c) Optical image of the sample achieved by the PDMS transfer process on the same black background. On the right are SEM images of the patterns at the bottom of the PDMS.

As a result, the SiO_2-NP/PDMS composite device appears completely transparent and the printed pattern is not identifiable, even on a white and blue background as shown in Figure 2-

2. The SEM images show the bottom sides of the SiO_2-NP/PDMS composite device. We can see that the coffee-ring patterns on the glass substrate are well transferred to PDMS integrally, which is further proved by the magnified SEM image. Furthermore, we can see that the SiO_2-NP/PDMS composite device is highly flexible and even stretchable, allowing the imposition of multi-modal mechanical stimuli to the device as shown in Figure 2-2b.

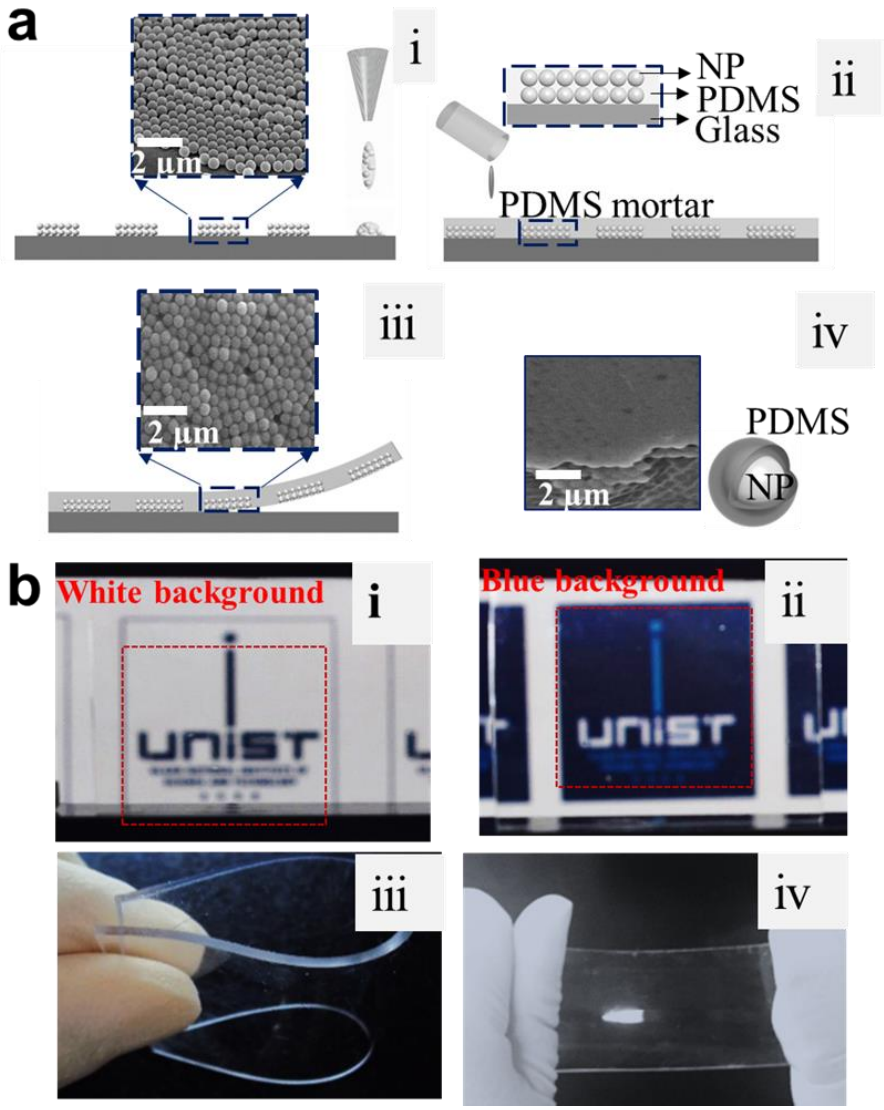

Figure 2-2. Fabrication process of the structurally switchable coloration device and characterization. (a) Fabrication process of the device. Inkjet-printed NPs are self-assembled on a glass substrate in a coffee-ring fashion, and then PDMS mortar is casted and cured. Then, the NP-encapsulated PDMS slab is peeled off, producing a transparent and flexible device. The SEM images

show the nanoscopic structure of the device. (b) The device enclosed by a dashed-line rectangle in (b)(i) and (b)(ii), respectively, shows high transparency against a white background and a blue background. In addition, the device shows high flexibility in the case of bending (b)(iii) and stretching (b)(iv).

Figure 2-3 illustrates the structurally switchable coloration mechanism of the SiO_2-NP/PDMS composite device when the device is subjected to different external stimuli. As shown in Figure 2-3a, the SiO_2-NP/PDMS composite device is completely transparent in the normal state because of the similar reflective index values of SiO_2 and PDMS. In addition, the corresponding SEM images of the surface morphologies validate the transparent mechanism of the device. In particular, periodic wrinkle patterns are entirely absent, and therefore, the device generates no grating structures and does not interfere with light. Interestingly, the SiO_2-NPs are well encapsulated with PDMS and their lattice structures are clearly seen in the SEM images (enclosed within the green and purple rectangles). Figure 2-3b shows the colorful image of the "UNiST" logo that appears when the device is bent inward. The SEM images show that the compressive forces caused by the inward bending induced the SiO_2-NP/PDMS hierarchical composite surfaces to generate a periodic array of wrinkles along the y-axis, which resembles the surface morphologies of some insects[60] and plants.[61] The array of wrinkles behaves as a one-dimensional (1-D) diffraction grating by splitting the white light source into a spectrum of light of various colors (refer to Figures 2-3d and e). Thus, the transparent device in the neutral condition exhibits iridescent colors when the device is bent, and the colors depend on the viewing angle. The enlarged SEM images clearly show a grating structure with a periodicity of approximately 4.21 μm as indicated with the green and purple rectangles. In contrast, when the SiO_2 NP/PDMS composite is bent in the opposite direction (outward), the device does not display any color. This can be attributed to the fact that the array of wrinkles is not generated in the SiO_2 NP/PDMS hierarchical composite laminate in response to this external stimulus

(Figure 2-3c). In the same fashion as before, the SEM images show the deformation of the NP lattice structure in which the tensile stress can relocate NPs but cannot generate any periodic array of wrinkles.[62]

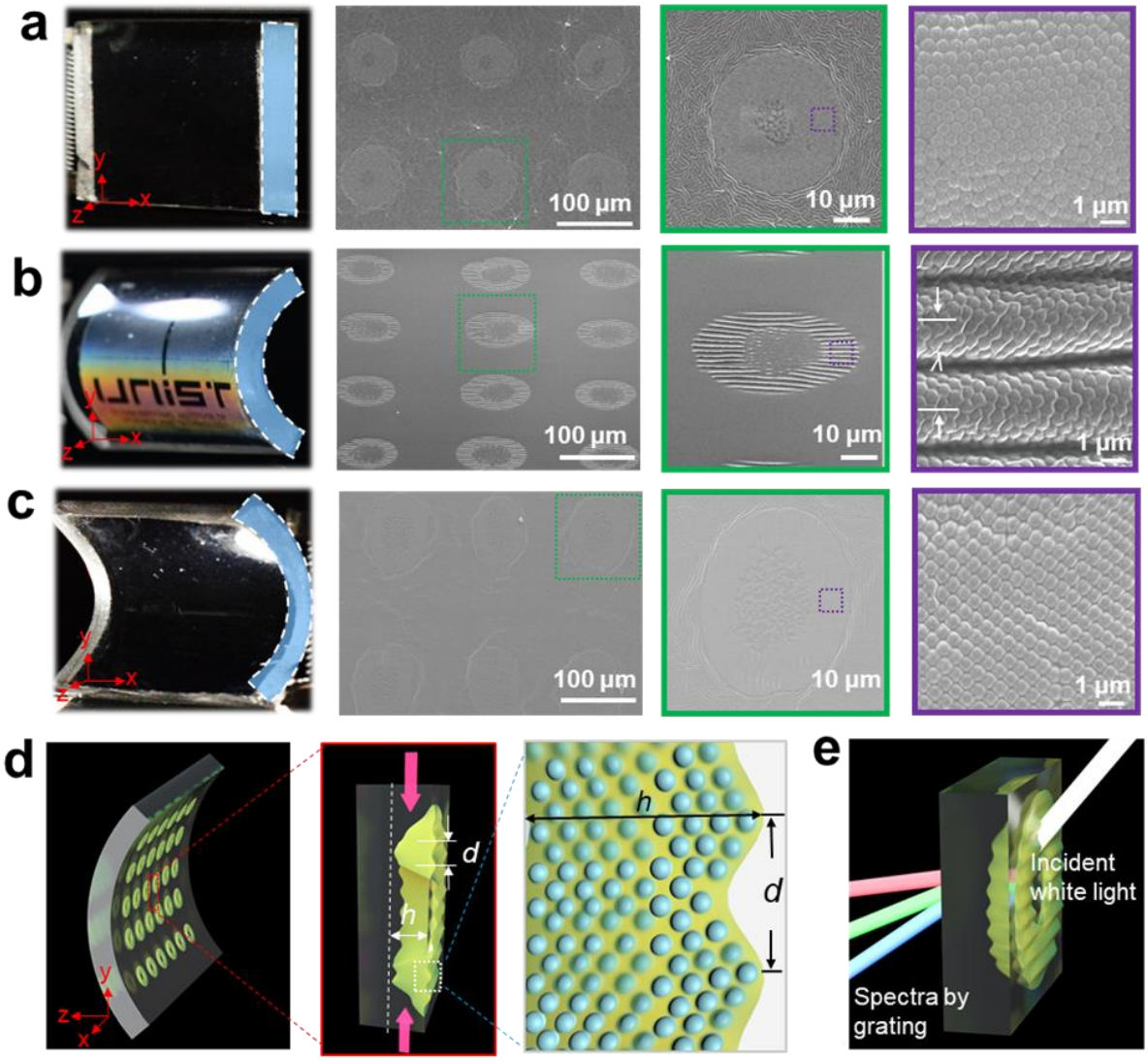

Figure 2-3. Structural coloration mechanism of the SiO_2-NP/PDMS composite device. (a) Optical image of the SiO_2-NP/PDMS composite device in the normal state (i.e., without external mechanical stimuli). The SEM images on the right show the patterns at the bottom of the PDMS. (b) Optical image of the same device when the patterned side is bent (inward). The SEM images show the patterns undergoing surface deformation and generating a 1-D array of periodic wrinkles. (c) Optical image of the same device when the patterned side is bent in the opposite direction (outward). The SEM images show wrinkle-free patterns. (d) Schematic of the surface wrinkle generation mechanism, in which the

different material properties of soft PDMS and hard SiO_2-NPs are essential. (e) Schematic of the structural coloration mechanism in which the array of wrinkles functions as a 1-D or 2-D grating.

We further investigated the effect of the shapes of the nanostructures on the generation of wrinkles by producing three representative nanostructural shapes: monolayer, coffee-ring, and dome-shaped nanostructures.[16, 63] Figure 2-4 shows the SEM and optical images of the three cases. These results indicate that the monolayer- and coffee-ring-shaped nanostructures are almost completely transparent when in the neutral position and that the colors are displayed when the structure is bent inward. However, for the dome-shaped nanostructure, the SiO_2-NP/PDMS composite device appears slightly whitish and displays no colors when bent inward or outward. This can be attributed to either the presence or the absence of the grating structure when bent, showing good agreement with all the experimental results in Figure 2-3. The SEM images of both the monolayer and the coffee-ring nanostructure show a distinct array of wrinkles on the PDMS surface. In contrast, the dome-shaped nanostructure seems to be tightly self-assembled and to have no room within which to compress or expand when an external bending moment is applied. Therefore, the SEM images show that the bottom surface of the device does not have any wrinkles.

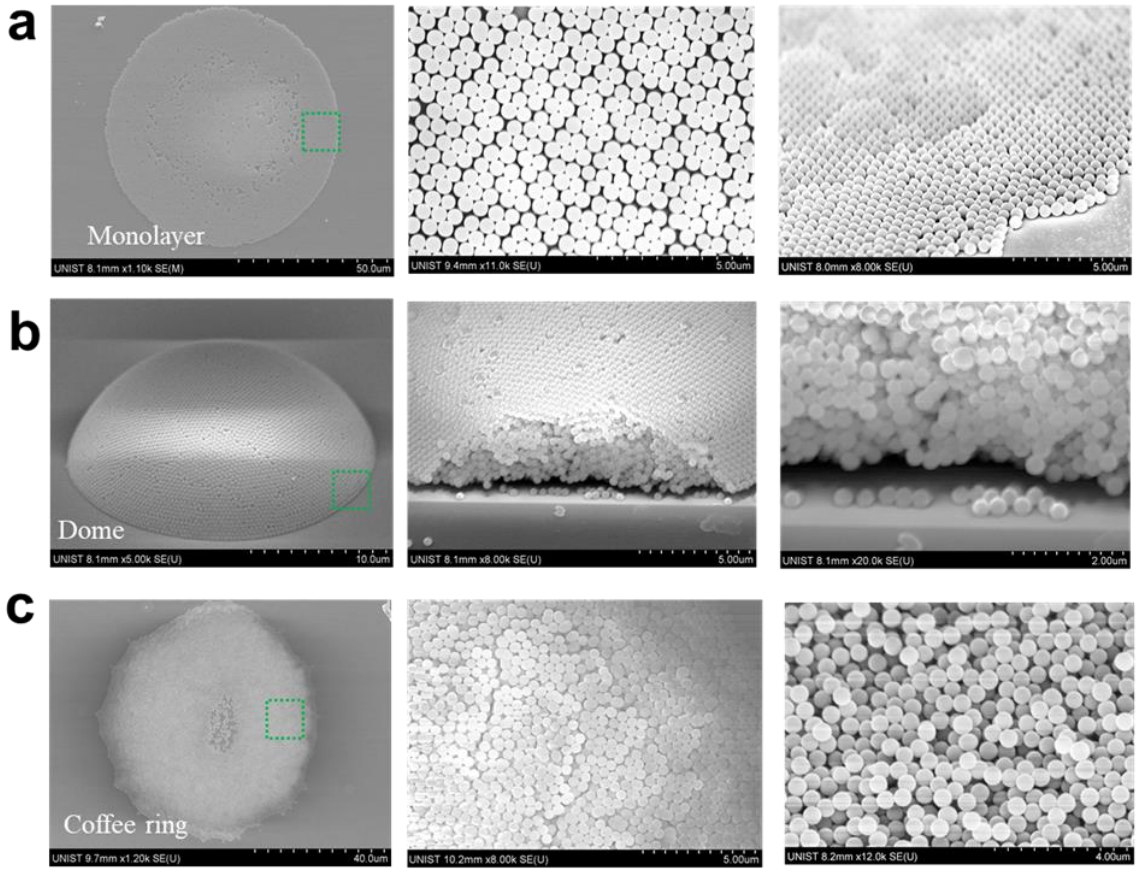

Figure 2-4. SEM images of the structures obtained by self-assembly of SiO_2-NPs. (a)–(c) Three different SiO_2-NP nanostructures for which self-assembly results are significantly varied but fairly controllable. The monolayer and dome-shaped nanostructures seem to be close-packed. However, the coffee-ring nanostructure seems to be coarsely self-assembled, allowing PDMS mortar to penetrate the nanopores.

Figure 2-4 shows additionally magnified SEM images of the nanostructures. That is, the particles in the upper layer on the surface of the coffee ring are not compact and the layer contains numerous voids. However, particles in the dome-shaped pattern are arranged more densely and tightly. The coffee-ring or monolayer SiO_2 NP pattern allows PDMS to permeate into the gaps between the SiO_2 NPs and form a composite structure in the form of a more rigid film. However, it is not easy for PDMS to penetrate the openings in closely packed SiO_2 NPs in domes. Therefore, the SiO_2 NPs in the dome-shaped nanostructure remain as an entire large

block with a very high Young's modulus, thereby causing the periodicity of the wrinkle pattern to be larger than that of the dome pattern. Therefore, no wrinkles can be observed at the microscale level. Specifically, the coffee-ring nanostructure displays the most vivid coloration even in sunny outdoor environments, as shown in Figure 2-5, thereby showing the remarkable potential of our device for various applications.

Figure 2-5. Performance of the structurally switchable coloration device in sunny outdoor environments. The device consisting of a coffee-ring-shaped SiO_2-NP nanostructure array shows the most vivid colors, even working well in sunny outdoor environments.

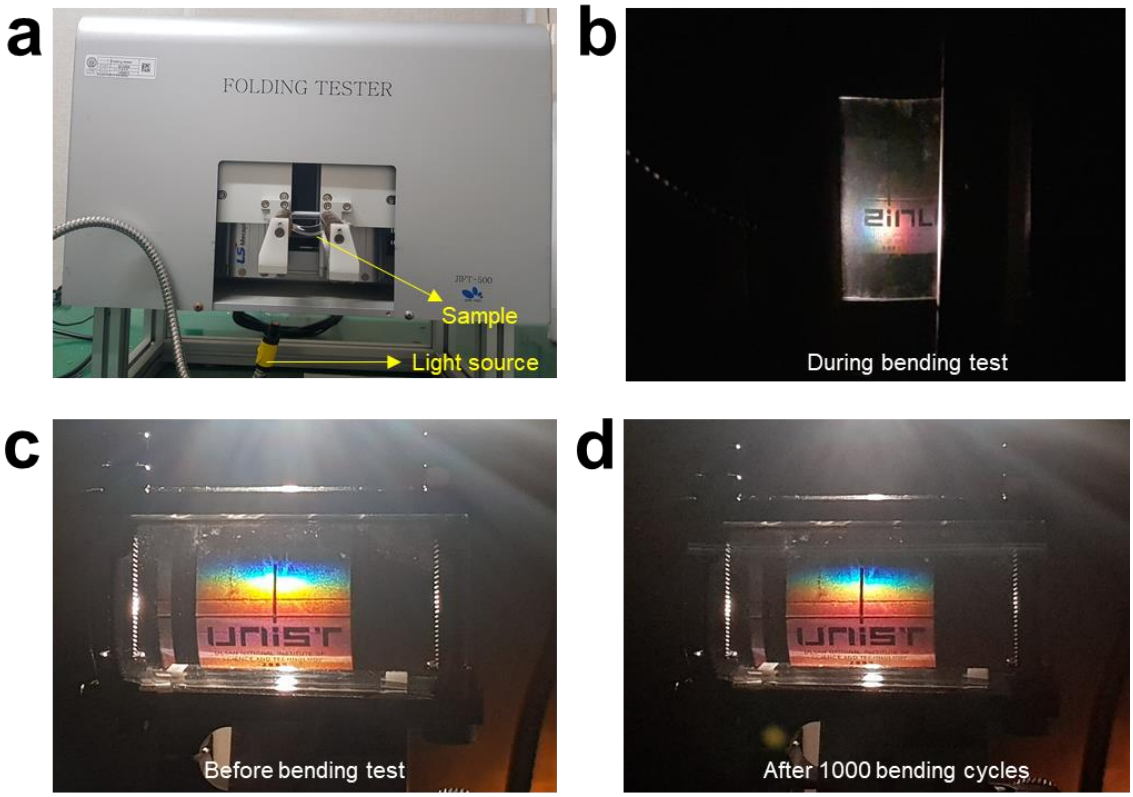

Figure 2-6. Experiment of the fatigue resistance property of the coloration device. (a) Picture of the experimental setup for bending test. (b) Picture of the device taken during bending test. (c) Picture of the device before the bending test. (d) Picture of the device after 1000 bending cycles.

Generally, PDMS shows an excellent mechanical property in elasticity and flexibility so that, after 1000 times of cyclic bending tests, the PDMS-based structural color platform still worked well, showing its robustness in fatigue resistance property as shown in Figure 2-6.

Then, we clarified the mechanism of wrinkle generation to show that a thin and rigid film/layer on the surface of a thick and soft substrate/layer is corrugated when subjected to compressive loading, as shown in Figure 2-3d. More theoretically speaking, buckling-type instability occurs only in the film because of a mismatch between the mechanical properties of the thin rigid film and the soft thick substrate, leading to the formation of an array of wrinkles/pattern with a certain amplitude.[64] In the similar manner, wrinkles are generated by depositing a layer of metallic thin film (i.e., rigid) onto the partially deformed shape memory polymer surface (i.e., soft) and then following a shape recovery process.[65] In this work, an array

of periodic wrinkles was generated only for the monolayer and coffee-ring-shaped nanostructures when the device reaches a new equilibrium state, which depends on the applied compression.[66] The periodicity λ of the array of wrinkles is determined by the thickness (h) and Young's modulus (E_f) of the film and Young's modulus (E_s) of the substrate as predicted by the linear bulking theory as follows:[26, 27]

$$\lambda = 2\pi h \sqrt[3]{\overline{E_f}/\overline{E_s}} \qquad \text{Eq. (1)}$$

where $\overline{E}$ is the plane-strain modulus, defined as $E/(1-v^2)$ with v being Poisson's ratio. Eq. (1) models the surface wrinkling phenomenon and allows us to predict the periodicity of our device. More specifically, the SiO_2-NP/PDMS composite film can be considered to be a rigid film layer because Young's modulus of the SiO_2 NPs (the value of E_f is dozens of GPa) is much higher than that of the soft PDMS substrate (E_s = 0.75 MPa). The PDMS surrounding the coffee-ring nanostructure exerts a compressive force as shown by the red arrows in Figure 2-3d. Figure 2-3e shows the structural coloration mechanism in which the wrinkle array functions as a 1-D or 2-D grating.

Figure 2-7. The influence of the bending degree of the device on coloration. (a)–(c) Three different bending degrees such as 'small', 'intermediate', and 'large' from left to right were tested and resulted in the similar coloration. This is because the wavelength of the winkles generated by these bending conditions exceeds the critical value in the winkle distance spacing, resulting in the similar iridescent coloration.

Additionally, we investigated into the effect of the thickness and bending degree of the device on coloration. In fact, these two parameters are correlated with each other because the thinker the device the more bending occurs. First, we prepared a regular coloration device with the same length and width as shown in Figure 2-7. And then we manipulated the bending degree in three ways such as 'small', 'intermediate' and 'large' by changing the gap distances between the top and bottom plate of the sample holder. From this experiment, we could see that the iridescent coloration seems to be almost the same and is not affected by the bending degree. This is because, when the compressive stress exceeds a certain threshold, the winkle spacing does not significantly change any more, resulting in that the wavelength of the wrinkles generated on the surface of the devices is independent of the applied stress. The further increase of the applied stress is known to affect only the amplitude of the wrinkles rather than the wavelength.[66] Of course, a slight difference may be caused by the change of the bending curvature of the device under different bending conditions, affecting viewing angle-dependent coloration. Second, we fabricated three coloration devices with the same length and width but different thicknesses such as 0.5, 2, and 5 mm as shown in Figure 2-8.

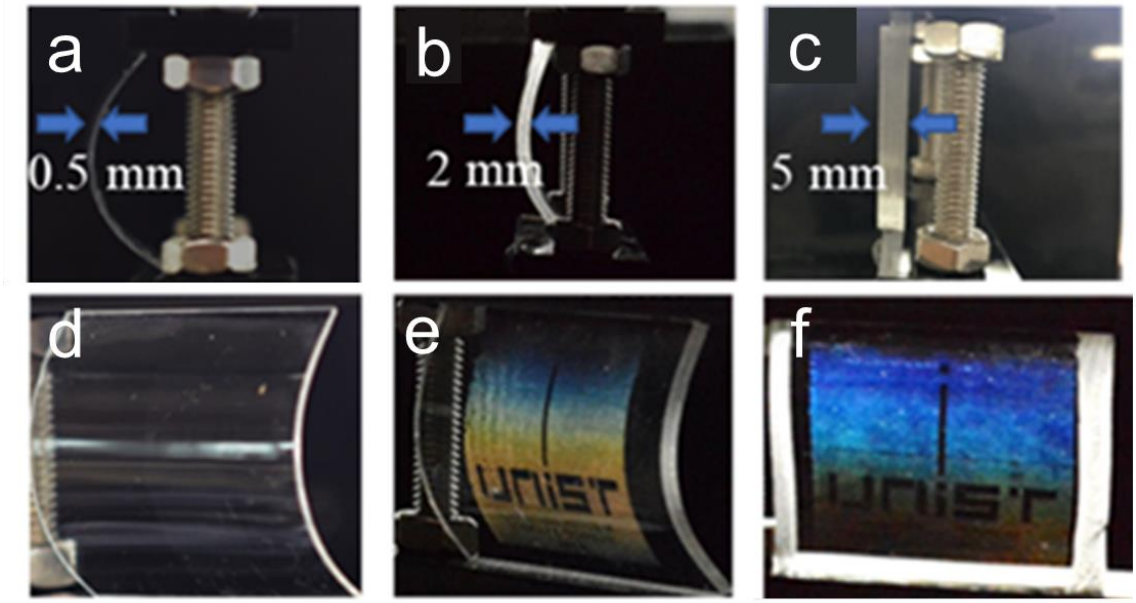

Figure 2-8. The influence of the device thickness and bending degree on coloration. (a)–(c) Side views of three samples with different thickness (e.g., t = 0.5, 2, and 5 mm) and different bending degrees such as 'large, 'intermediate', and 'small'. (d)–(e) Front views of the device corresponding to (a)–(c), respectively. The thinner the longer the wavelength of the winkles while the thicker the shorter. (d) No periodic winkles are generated. (e) Winkles are generated and display iridescent colors. (f) The thick device can easily generate surface winkles under a small bending condition, resulting in coloration.

When the devices were bent at different bending degrees such as 'small', 'intermediate', and 'large', the coloration difference is obvious. For the thinnest device, no colors were seen because no winkles were generated even under a 'large' bending degree. In other words, the compressive stress applied to the inner surface of the device was insufficient to generate surface wrinkles because the wavelength of the winkles did not reach a threshold for coloration. On the contrary, it is interesting that, for the thickest device, the threshold could be reached even at a 'small' bending degree, thereby resulting in the iridescent coloration.

Figure 2-9 shows the results of further experiments to characterize the structurally switchable color platform. First, SiO_2 NPs with different sizes were used to print and create similar structural color platforms. The SEM images in Figure 3a through 3c show that when printing

coffee-ring patterns with SiO_2 NPs with a size of 300 nm, the periodicity of the wrinkles is approximately 2.44 μm. Correspondingly, when printing coffee-ring patterns with 700 nm SiO_2 NPs the periodicity of the wrinkles is approximately 6.85 μm. The increase in wrinkle periodicity with the increase in particle size can be explained by the increase in the thickness of the thin hard film (*h*) as the particle size increases. At the same time, the corresponding optical images indicate the occurrence of an obvious red shift when the particle size increased from 300 nm to 700 nm. This can be explained by the diffraction equation,[67, 68] $n\lambda_w = d(\sin\theta_D - \sin\theta_I)$, where the integer n is the order of diffraction; λ_w is the wavelength of white light ranging from 400 nm to 700 nm, which almost covers the visible color spectrum; θ_D and θ_I are the observation angle and incidence angle, respectively, which are fixed during the experiment; and *d* is the period of the wrinkles. Thus, red shift is expected to occur as the periodicity of the wrinkles (the value of *d*) increases with the particle size.

As shown in Figure 2-9d through 2-9f, the diffraction spots were taken from the structural color platform with different SiO_2 particle sizes. When the samples are bent inward, linear spot arrays with different distances can be obtained. The experimental setup for diffraction measurement is illustrated in Figure S8a. However, diffraction spots do not appear when the structural color platform is bent in the opposite direction (outward) or without bending (Figures S8c and d). The following information can be obtained from the results. First, the grating effect is mainly contributed by the SiO_2 NP/PDMS hierarchical composite wrinkles rather than the SiO_2 particles. Second, the distance between wrinkles can be calculated by using the following equation,[50]

$$d = \frac{4\lambda_{laser}\sqrt{(D/2)^2 + L^2}}{\sqrt{3}D} \qquad \text{Eq. (2)}$$

where λ_{laser} is the laser wavelength, d is the wrinkle spacing, L is the distance from the screen to the structural color platform, and D is the distance between diffraction spots from the same order of diffraction. Using the diffraction spots and the distance taken from structural color platforms created using SiO_2 NPs with different sizes (300 nm, 500 nm, and 700 nm), the calculated values of the wrinkle periodicity are 2.99 μm, 4.92 μm, and 6.50 μm, respectively. These calculated values are close to the wrinkle spacings measured from the SEM images in Figure 2-9. Importantly, no voids are observed in the SEM images, supporting that the coloration is not caused by the void formation around the SiO_2 NPs. This also shows good agreement with the fact that the device does not display any colors when bent outward while compressive and tensile stresses may affect the void formation in the similar manner.[31] As a direct proof, we replicated the surface wrinkle array of the device on compression to a UV-curable PUA film on the PET substrate as shown in Figure 2-10. From the corresponding AFM image of the replicated PUA film, we validated again that the surface wrinkles play the key role in coloration as grating not the inside photonic crystals. As expected, the replicated PUA film displayed similar colors to the device. These results further confirm that the grating effect is mainly contributed by the SiO_2 NP/PDMS hierarchical composite wrinkles rather than by the NP lattice structures, which is negligible.

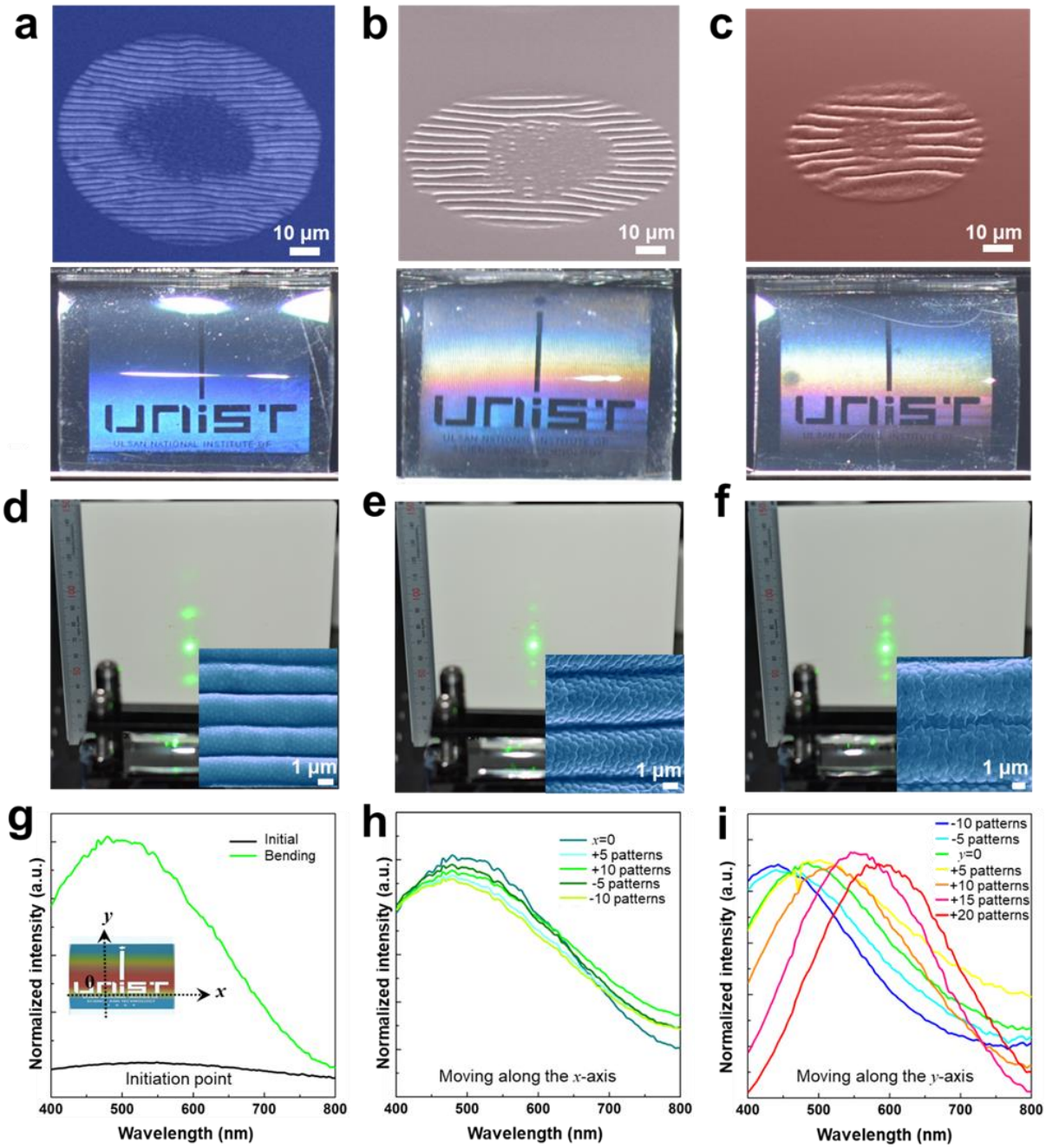

Figure 2-9. Optical characterization and analysis. (a)–(c) Three different structural coloration devices fabricated with SiO_2 NPs with different sizes: 300, 500, and 700 nm, respectively. Wrinkle morphologies and corresponding optical images are shown. (d)–(f) Diffraction spots are taken from the three devices in the same order of the particle sizes (i.e., 300, 500, and 700 nm, respectively). (g) Transmission spectra measured in the normal and inward-bent states. The sample was fabricated using 500 nm particles and the geometrical center was set up as the origin. (h) and (i) Transmission spectra measured by moving the device from the center in increments of five nanostructures/patterns along the

x- and *y*-axes, respectively. The center-to-center spacing distance between neighboring nanostructures/patterns are uniformly spaced approximately 150 μm apart.

Subsequent optical analysis of the structural color platform created by SiO_2 NPs with a diameter of 500 nm was carried out by using a UV-Vis microspectrometer (refer to Figure 2-10b). Figure 2-9g shows that an obvious peak appears in the visible range in the transmission spectra after bending owing to the grating effect caused by the resulting wrinkles. A series of spectra were recorded by moving the sample along the *x*- and *y*-axes, respectively. Figure 2-9h shows that the spectra remain almost constant when moving along the *x*-axis. This is because of the fixed *y*-coordinate; that is, the angle of incident light is the same and the geometry of the resulting wrinkles is similar because the bending moment along the *x*-axis remains the same. On the other hand, when moving along the y-axis, the shapes of the spectra change because the angle of incident light relative to the wrinkles changes as shown in Figure 2-9i. The iridescent colors captured with a CCD camera and shown in Figure 3c are in good agreement with the transmission spectra measured in Figure 2-9i. The farther the measurements were taken from the *y*-axis, the more dominant the red shift became. In Figure 2-11, we demonstrate a potential application of the structurally switchable color device that depends on the viewing angle. The iridescent colors become transparent when the device is rotated by 90° (Figure 2-11a). This is because the wrinkles are generated in a 1-D structure format when the device is bent along the y-axis (inward). After rotation, the grating structures diffract incident light into several beams travelling in different directions, which are tightly related to the winkle spacing and light wavelength. If the viewing angle is located outside of the space/area through which no beam can pass or multiple beams can pass, resulting in observing either transparency (i.e., no beam) or whitish coloration (multiple beams).

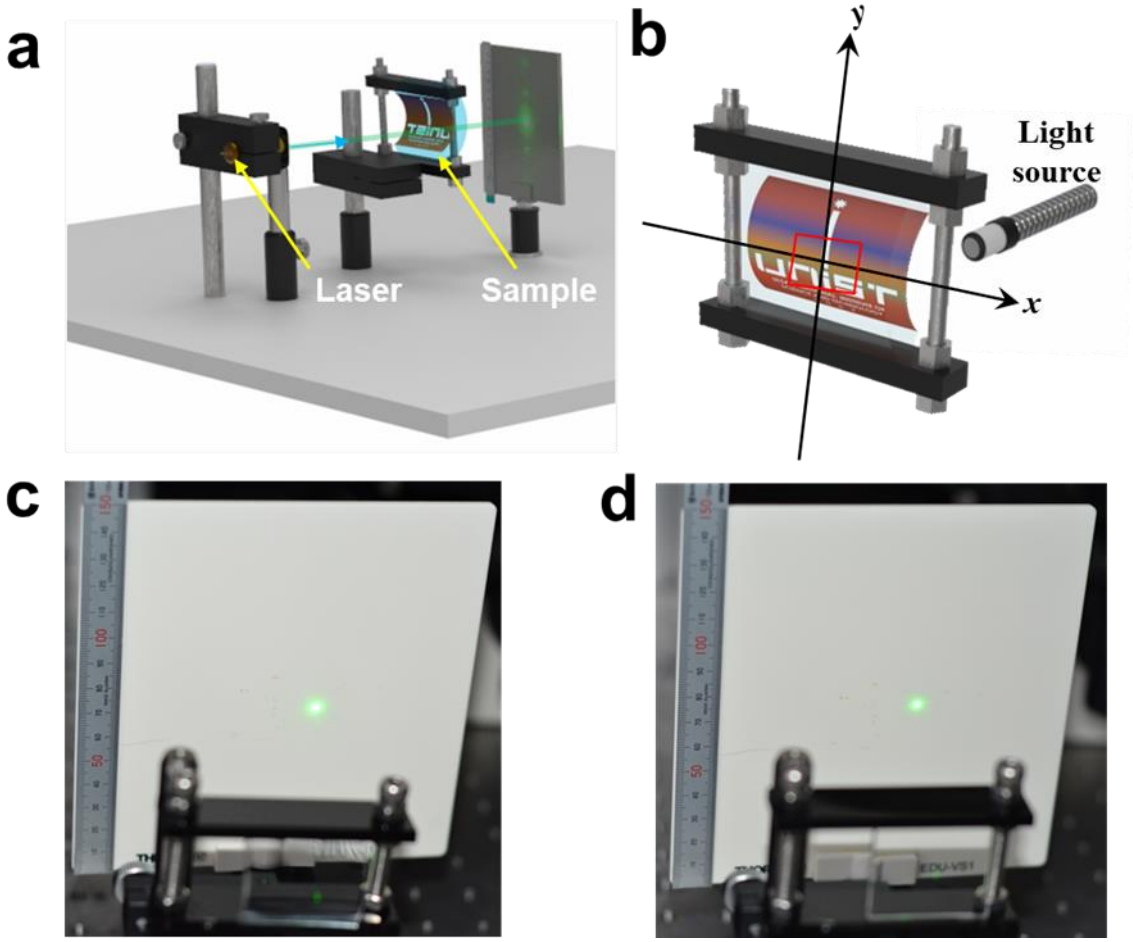

Figure 2-10. Optical characterization and analysis. (a) Illustration of the experimental setup to measure the diffraction pattern consisting of a laser source, a sample in the middle of the setup, and a white screen. (b) Illustration of the experimental configuration for optical characterization of samples/devices. Transmission was measured by fixing the light source but relocating the detection spots. (c) No diffraction spots were taken from the structurally switchable coloration device when it was bent outward, which was in the direction away from the detector. (d) The same experiment was conducted when the device was in the normal state (without any bending). Particle size was 500 nm.

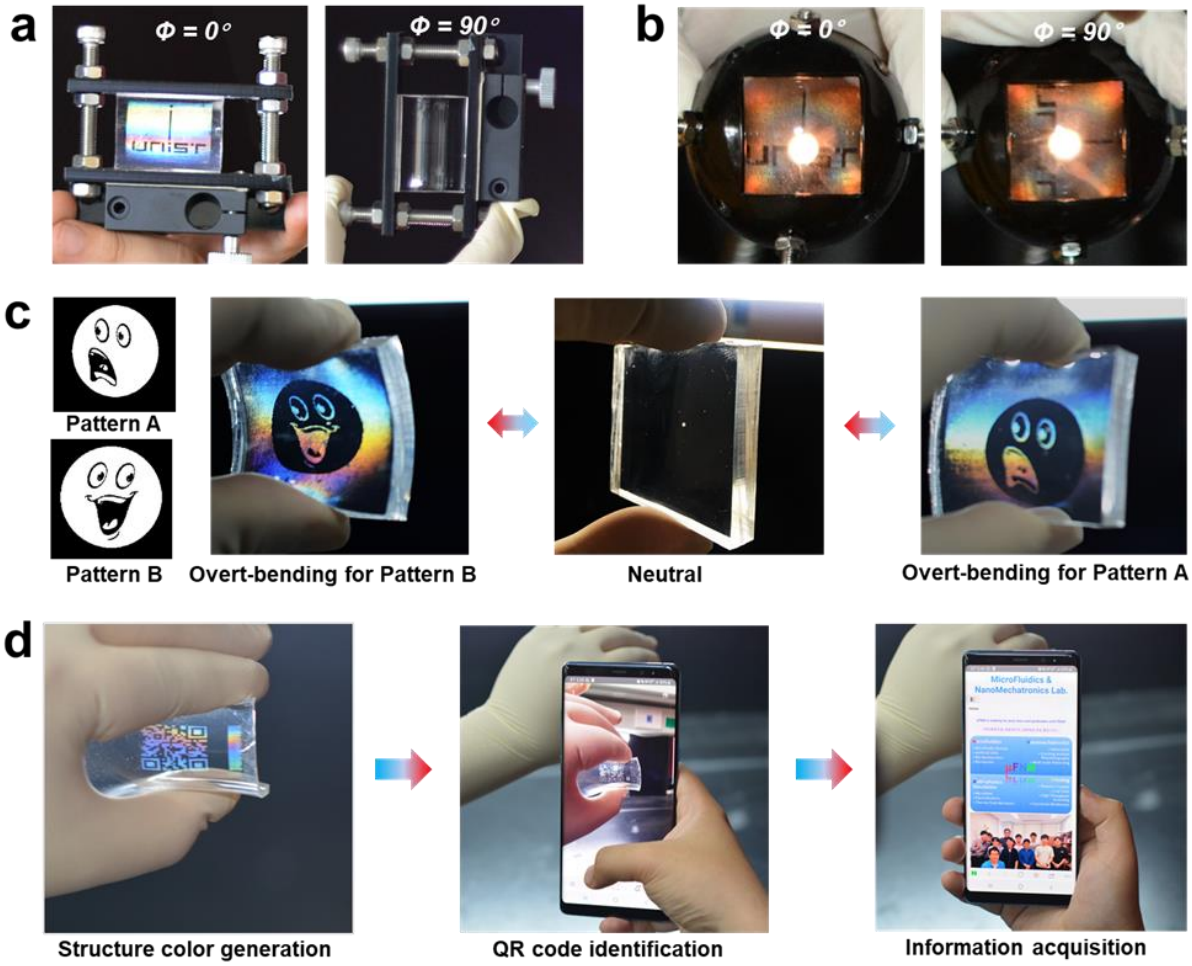

Figure 2-11. Application of the structurally switchable coloration device to multi-dimensional and multi-modal displays and anti-counterfeiting techniques. (a) Demonstration of viewing angle dependency of the coloration features device; that is, it displays an iridescent colourful image that disappears after 90° clockwise rotation in the case of a fixed light source. (b) The structurally switchable coloration device displays an iridescent image under isotropic pressure, which remains after 90° clockwise rotation for a fixed light source. (c) The same device with two different SiO_2-NP-encapsulated PDMS patterns on its two sides displays the corresponding optical images under inward and outward bending conditions. (d) A QR code pattern implemented on the device and the decoding process of the QR code with a regular mobile phone directly leads to the predefined website.

This phenomenon is caused by the lack of the symmetry and angle dependency of the structural color platform. [27]This feature enables the device to display colors only in a specific angle range, thus enhancing the confidentiality of information to meet the needs of specific

situations. Figure 4b shows that when an isotropic (2-D) compressive force is applied evenly to the sample, the colors induced by bending have a similar distribution even after the sample is rotated clockwise by 90°. This is because the generated wrinkles can change from a parallel 1-D structure array to a 2-D divergent structure (Figure 2-12).

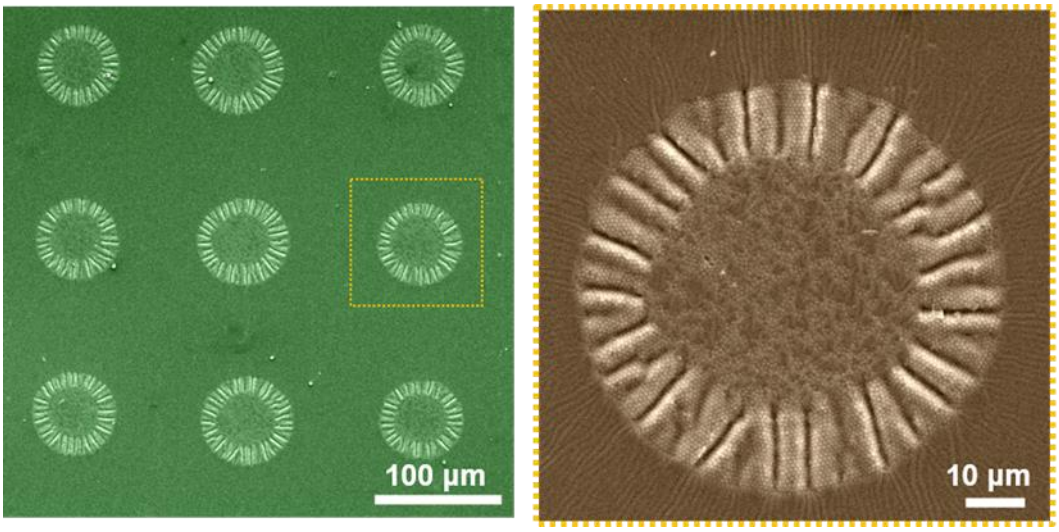

Figure 2-12. Wrinkle morphologies of the samples under isotropic stress. A spherical shell was used to achieve the isotropic force.

A spherical shell was used to achieve the force situations mentioned above. The transitional state was obtained by placing the structurally switchable color platform in a square box which enables a force to be applied from four perpendicular directions. The color distribution follows the force direction as well. In this case, 2-D twisted wrinkles resembling the gullies of the brain were generated (Figure 2-13). All these results prove that the structure and dimension of the wrinkles is sensitive to an external force and can be controlled freely. At the same time, as shown in Figure 2-14, the multi-modal structural color platform is also effective when subjected to stretching, as it can also generate weak wrinkles when stretched as a result of both compressive and tensile stress (Figure 2-14e).

Friendly and sad faces were printed and transferred to the different sides of a PDMS slab as shown in Figure 4c. When the PDMS is bent from one side, a colorful smiling face is revealed while the other (sad) face remains hidden. However, bending the PDMS in the opposite direction reveals the sad face while the smiling face is hidden. This result provides good evidence that the structurally switchable color platform is fully covert–overt convertible. It also

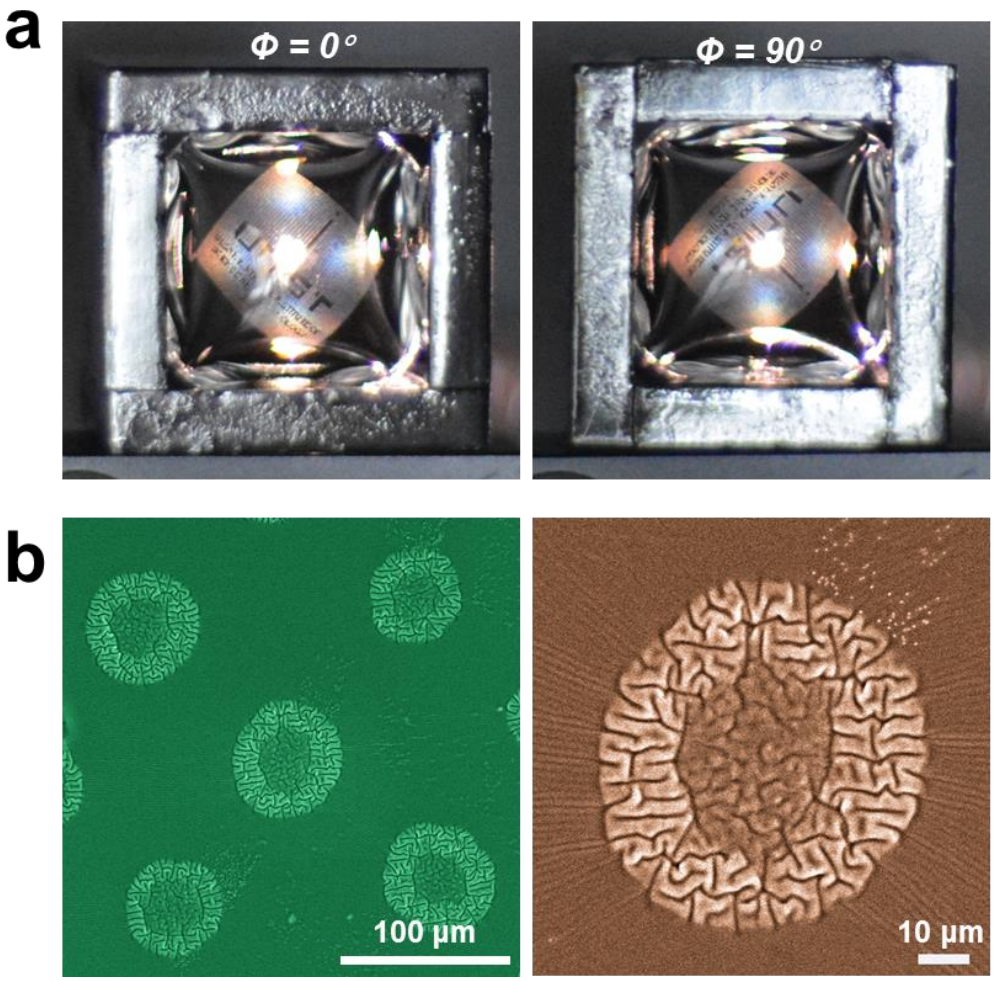

Figure 2-13. Coloration and wrinkle generation results of the structurally switchable coloration device when a 2-D compressive force is applied using a square frame. (a) The coloration result before and after 90° clockwise rotation of the device. (b) Scanning electron microscopy (SEM) images of the surfaces of the device show axisymmetric wrinkle patterns; in fact, the 2-D compressive force applies isotropic compressive stresses to the device.

clearly indicates that two independent structurally tunable colors can be incorporated in a single platform. The quick response capability is another advantage of this platform compared with others.. In addition, this structural color platform could be used in an anti-forgery system based on QR codes as shown in Figure 2-11d. As a form of 2-D bar code, QR codes have some remarkable advantages, including fast speed, large storage capacity, and high error-correction capability.

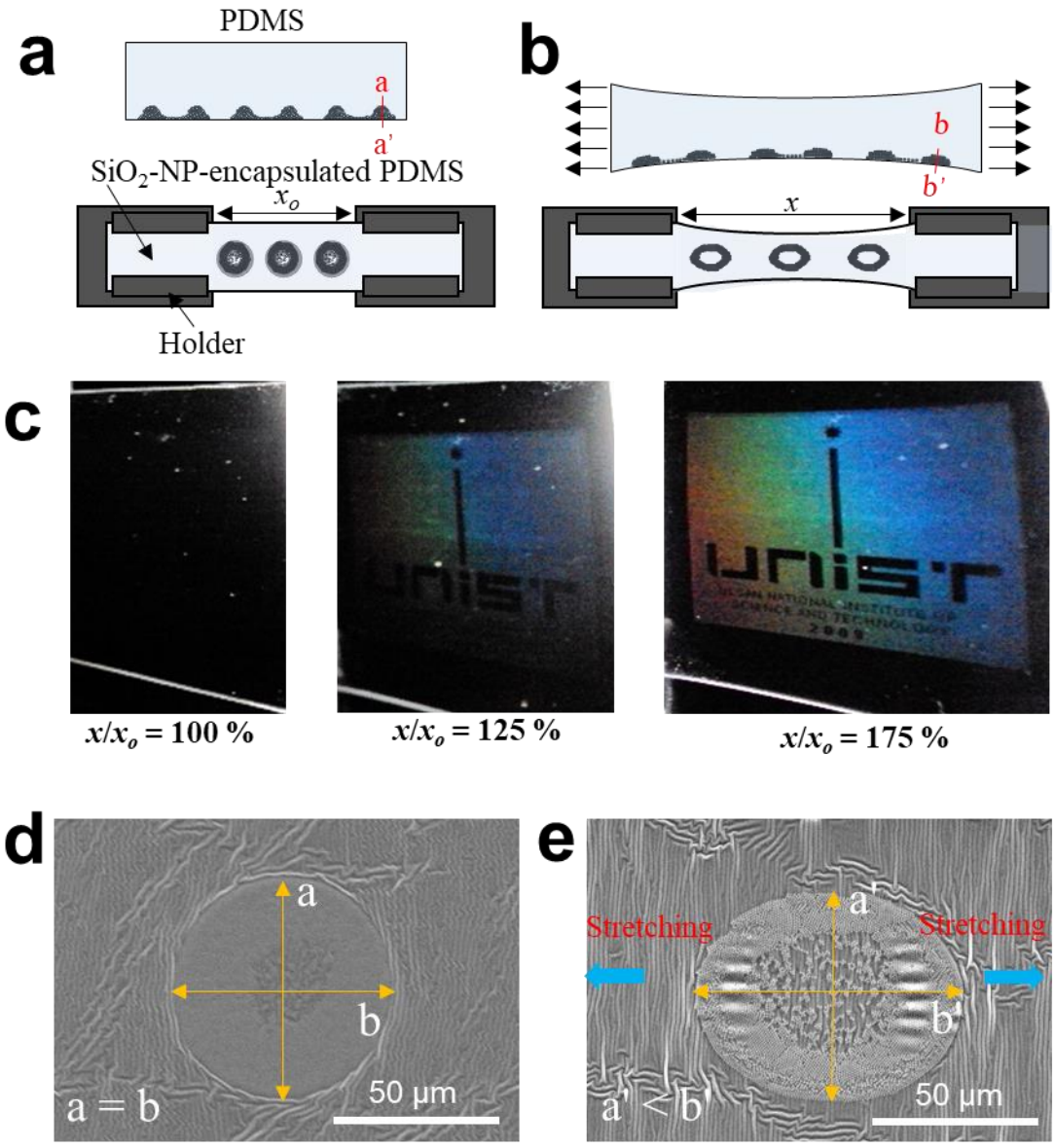

Figure 2-14. Operation of structurally switchable coloration device subjected to mechanical

stretching. (a)–(b) Schematic of the SiO_2-NP-encapsulated PDMS before and after stretching (upper: side view and lower: top view). Before stretching, the PDMS device is fully transparent. However, stretching the device causes wrinkles to form, thereby displaying iridescent colors. This is because the circular coffee-ring-shaped structures undergo 2-D mechanical stress; that is, tension along the x-axis and compression along the y-axis. (c) Images captured by a charge-coupled device (CCD) camera: no coloration (neutral, left) and with coloration (middle and right). Viewing-angle-dependent and rainbow-like iridescent coloration is shown along the x-axis. (d)–(e) SEM images of the surfaces of the device before and after stretching. A circular SiO_2-NP-encapsulated PDMS surface in (d) is transformed to an ellipsoidal one (a' < b').

The most important advantage is that this technique converts the original information (such as text and an image) into a binary 2-D image that can be easily processed by various kinds of information processing applications.[69] Thus, QR codes have been used in a broad context, including in both commercial tracking applications and convenience-oriented applications aimed at mobile-phone users (termed mobile tagging). However, in certain situations it would be undesirable to publicly display the QR code. The structurally switchable color platform could be useful in such a situation. To verify the applicability of the structurally switchable color platform to use QR codes to retrieve hidden information, we prepared such a platform with a QR code. Then, a commercially available smartphone on which a custom-developed app was installed was used to recognize the QR code. Under a compressive force the clear QR code can be identified by the smartphone, which displays the encoded information, i.e., the home page of the authors' laboratory. Furthermore, two independent structurally tunable color devices with different QR codes were incorporated in a single platform and assembled with an ID card. By bending the card in different directions, two different QR codes are displayed alternately. Correspondingly, two web pages could be successfully accessed (refer to Figure 2-15). For a practical application, instead of normal web pages, the information could be purpose-designed for the application. Thus, other applications such as tracking and anti-counterfeiting of products or drugs could also be realized in the same manner.

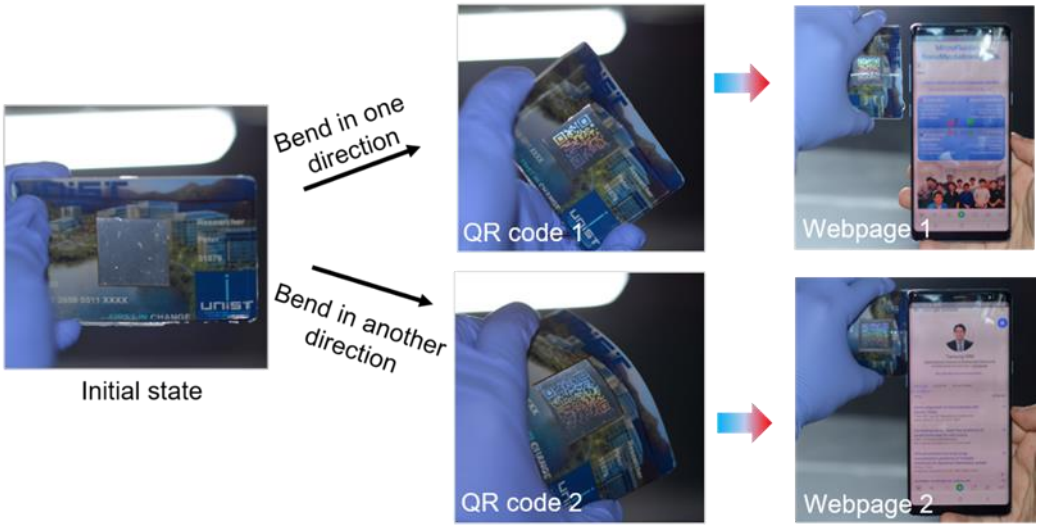

Figure 2-15. Anti-forgery system based on two QR codes on the two sides of a single structurally switchable coloration device. Demonstration of the process of decoding two different QR codes that were fabricated on the two sides of a single device integrated into an ID card. Selective bending of the ID card allows access to two different websites.

2.4. Conclusion

In summary, we developed self-assembled SiO2-NP patterns encapsulated by PDMS as a novel and simple color platform that is structurally switchable by applying external mechanical stimuli. The similarity of the optical properties of PDMS and SiO2 NPs are exploited to realize a fully transparent structurally switchable color platform in the normal state. However, owing to the large difference in mechanical strength, 1-D or 2-D arrays of wrinkles are generated on the surface of the laminate when subjected to different amounts of compressive stress based on buckling-type instability. In turn, the arrays act as multi-dimensional gratings to display various structurally switchable colors depending on the viewing angle. We attributed the iridescent coloration to only the wrinkles rather than the SiO2 NPs by measuring the light transmitted through or diffracted by the gratings. We demonstrated that the platform could be applied to develop anti-counterfeiting techniques in which two covert QR code patterns could be selectively transformed to become overt under compressive bending from different directions. The entire process is easily achievable by combining finger-based mechanical stress and the CCD camera with which mobile phones are equipped. Hence, we successfully demonstrated structurally tunable color-based optical encryption/decryption of multiple pieces of information. At the same time, because of its initial transparent state, it is possible to combine this laminate with flexible electronic devices. All of the above show its remarkable potential for anti-counterfeiting applications in a simple, convenient, inexpensive, and mass-producible manner.

Chapter 3 Trilayer Film

3.1 Introduction

Micro- and nanoscale wrinkles naturally formed on soft materials inspired by nature material have attracted wide attention due to their lithography-free and simultaneous fabrication process with nanometers to micrometers on scale [70-73]. These unique instability behaviors reveal notable intrinsic structure features of high surface to volume ratio, periodicity, compatibility[66]. Due to these advantages, study of wrinkles has gained great interest in various research fields, such as stretchable device[74], optics[75], anticounterfeit[76]. The main strategy is to mimic the skin structure based on the inhomogeneity of the bilayer film caused by external stimuli such as mechanical[77], chemical[78], and thermal stresses[79]. When stress factors induce the inhomogeneity of a stiff layer and a ductile substrate, which are typically applied to the bilayer system above a certain threshold, the stiff thin layer undergoes material deformation and surface-structural change during the deformation of the ductile substrate.

Recently, bilayer structures comprising combinations of polydimethylsiloxane (PDMS) and various stiff film materials, such as metals[12], 2D materials[13], and polymers[14] have been extensively studied. Although wrinkles formed on the bilayer film have been studied, incorporating the desired characteristics in periodic nano-wrinkles is challenging. Controlling wrinkle size depends on difficult-to-modulate inherent parameters (e.g., elastic moduli of the stiff films and ductile substrates, and strain rates). Therefore, fabrication approaches to forming polymorphic and multiple wrinkles are mainly limited to patterning materials with different thickness instead of modulating the material properteis. There are many existing fabrication methods such as selective UV curing[80], local oxidation[81], thickness gradient of a metal layer[82], template structure[83]. However, they are either too complex and/or unable to adjust the thickness of each layer to be laminated in a continuous and accurate manner. On the other hand, the

diffraction efficiency depends on the amplitude of the wrinkles; that is, the higher the amplitude is, the clearer the structural colors are shown[84]. However, the amplitude is largely affected by the magnitude of the applied stress. Unfortunately, for the bilayer film structure, the increase of external stress plays a key role in generating the surface wrinkle structure. It is not possible to increase the wrinkle amplitude only for specific pattern areas in cases of the most previous fabrication methods so as to make the color pattern clearer.

As an alternative to control the top surface morphology by external stresses, forming a triple layered film in which two layers are stacked on top of a soft and ductile bottom substrate has attracted attention. This is because the fabrication method allows to simply adjust the thickness of the stacked layers, thereby resulting in the thickness inhomogeneity of the film, which in turn causes not only the shift of the neutral plane of bending stress but also the surface strain differences[85]. However, the method does not allow to adjust the intrinsic mechanical properties (e.g., Young's modulus) and the patterning position on a substrate selectively. In other words, it seems to be hard to produce wrinkle patterns partially out of a substrate in a selective manner. Therefore, a novel method is highly demanded to generate the inhomogeneity of layer thickness and material property out of an entire device/substrate locally and selectively although such a method can spawn a variety of wrinkle-based applications[86, 87].

In this work, we present a transparent, flexible, and trilayer film that can actively display iridescent structural colors when compressive or bending stresses are imposed on. We fabricate the film by directly printing a chitosan solution on the bottom polydimethylsiloxane (PDMS) substrate, which results in an interlayer with different thickness. And then, we spin-coat the patterned substrate with a mixture of polyvinyl alcohol (PVA) and chitosan to embed the printed patterns, forming a trilayer thin film. We characterize the printed pattern, which is called an interlayer, to modulate the mechanical property of the interlayer to cause a local,

heterogeneous instability of the trilayer film. In addition, when compressed or bended, the film can generate periodic wrinkles that can be controlled precisely in a ten of nanometers in a multimodal manner. Lastly, we demonstrate a brand-new secured barcode system that can encrypt information using multiple colors but decrypt it in presence of a particular color filter. The material patterning technique developed in this work can be used as powerful tools for controlling wrinkles in various applications such as anti-counterfeiting systems, soft robots, and optoelectronics in the near future.

3.2 Materials and Method

PDMS Substrate preparation: PDMS were fully mixed with a weight ratio of 10:1 (base to curing agent), and then put into the vacuum for 30min to remove the air bubbles. After fully degassing, PDMS mortar was poured on the square dish, and fully cured in oven at 70℃ for 3hours. The height of the substrate film was controlled by the weight of the PDMS in the square dish of a specific size.

Inkjet printing: The pattern of chitosan structures on the substrates was prepared by using a piezoelectric drop-on-demand inkjet printer (DMP-2800, Fujifilm Dimatix, Inc., CA, USA) with a cartridge (Model No. DMC-11610). The center-to-center droplet spacing can be controlled from 5 μm to 254 μm by adjusting the angle of printer head in one-micron increments and dependent upon the resolution setting (9 dpi).33 The droplet spacing of varying 10 μm to 70 μm was maintained in whole fabrication in order to overlapping of droplets.

Reagent and materials: For preparing Chitosan ink, 0.1g of chitosan powder (Sigma Aldrich, Korea) and 100 μL of acetic acid (Sigma Aldrich, Korea) was mixed with 10mL of D.I. water, and stirred for 12 hours on the hot plate of 65℃. Then the Chitosan solution was diluted to specific concentration (0.07% w/v) for the final ink. For the Chitosan/PVA blended solution for the laminating film, Liquid type PVA (Polyscience, US) 0.75g was dissolved in 10ml of D.I. water for dilution to 1% solution. The final solution was prepared by properly mixing the chitosan solution and liquid PVA with a vortex mixer at a specific ratio according to the Young's modulus.

Printing conditions: Different intermediate patterns can be achieved by inkjet printing the chitosan solution (0.07% w/v) on the plasma treated 5mm thick PDMS substrates. The substrate

was first plasma treated (50W/30s) to increase the wettability (contact angle, CA = 15°) for uniform flat pattern by linking each adjacent droplets. Then, the inkjet printing has been conducted by varying the droplet distance from 10 μm to 70 μm in a 15-μm interval. By repeating the injection of droplets over and over at the same spot of patterns, the thickness of the intermediate patterns was modulated.

Spin-coating conditions: The height of the laminated layer has been modulated via the spin coating rate of the chitosan/PVA blended solution by using spin coater (SPIN-1200D, Midas system, Korea). 100 μL of chitosan/PVA solution has been put on the printed substrate, and spin coating with the spin rate of the 1000 rpm to 3000 rpm has been conducted. Then the sample was evaporated in the oven at 70℃ for 30 minutes.

Duplication: Generated wrinkles on the triple layered film while bended state has been duplicated for the flat wrinkled surface. 250 μm thickness of PET has been attached to the cylindrical bending glass mold, radius of 4.2cm. The optical adhesive, NOA63 (Norland products, USA) has been put on the triple layered film and attached directly to the PET. Then the custom-made device has been used to apply pressure to the film to maintain the bended state until the adhesive has been fully hardened by exposing to the ultraviolet rays of 15W, 365nm, using the UV hand lamp (UV-LF215L, Uvitec, England) for 30 minutes. Finally, all the devices and film has been removed, and the wrinkle duplicated surface of NOA63 on the PET has been gained.

Characterization: All the contact angles (CAs) reported in this study were measured by a goniometer (Smart Drops SDL200TEZD, Femtofab Co. Ltd., Pohang, Korea). Single deionized water droplet of 1μL was gently placed onto the glass substrates. The averaged value of the CA reported is the mean of 10 measurements of CA. SEM images were taken and utilized

to study the morphology and spatial distribution of the resulting wrinkles (S-4800, Hitachi, Japan). Two types of CCD cameras were used: SLR CCD camera (Nikon D300, Nikon, Japan) for high-quality images and Galaxy Note 20 (SM-N981N) for regular images. The wide spectra were collected using the UV−visible–NIR microspectrophotometer (20/20 PV UV−visible−NIR microspectrophotometer, Craic Technologies, San Dimas, CA, USA). A mobile phone, Samsung Galaxy Note9 (SM-N960N) and the commercial application of BARCODE SCANNER (Cognex, US) was used for barcode recognition tests.

3.3 Result and discussion

Figure 3-1a shows the main working concept of the trilayered, covert-overt, and transformable film that is completely transparent and flexible. The application of bending stress generates wrinkles on the surface of the film and produces structural colors because the wrinkles act as a diffraction grating with a periodic structure. Upon releasing the bended film, the wrinkles disappear and the film become transparent again. Figure 3-1b schematically illustrates the facile fabrication process of the material property patterning method by solution process. Firstly, by inkjet printing, ink droplets containing chitosan molecules were injected on a plasma-treated PDMS substrate. The reason why the PDMS surface needs oxygen plasma treatment is to obtain hydrophilic surface. In this way, the chitosan solution ink can spread quickly to form a film after printing. After the water volatilizes, a chitosan film with a nanoscale thickness is obtained because of the excellent film-forming property of chitosan24. At the same time, the film thickness can be actively modulated by simply adjusting the droplet spacing distance. In other words, the droplets are injected closely, they are overlapped on the substrate, resulting in a thick chitosan pattern. Figure 3-2 shows the relationship between the thickness of the chitosan interlayer and the spacing distance of injected droplets. As the injection spacing distance (i.e., the droplet spacing distance) decreased from 70 μm down to 10 μm, the thickness of the chitosan interlayer patterns increased linearly from 130 to 330 nm. . Although multiple droplets are injected repeatedly at the same patterning area, the printed chitosan pattern was horizontally uniform and tightly deposited on the substrate. After the complete evaporation of the chitosan droplets, these printed chitosan interlayer patterns show slightly opaque colors, depending on the printed pattern thickness. At the same time, in order to display the effect of thickness control more intuitively, red food dye or fluorescent dye (Rhodamine-B) was respectively mixed into ink and printed. From the optical photo in Figure 3-1c and the fluorescent image in Figure 3-

1d, it can be seen that the color depth of the pattern changes significantly with the change of thickness. If the trilayered film is transparent in the natural state, it can well hide important information. Thus, to hide the chitosan interlayer pattern, the difference between the refractive index of the top layer and chitosan shall be less than 0.05. Thus, a mixture of PVA and chitosan was spin-coated to fully laminate the chitosan interlayer. The reasons for choosing a mixture of PVA and chitosan are as follows. First, the reflective index (R) of each thin film made of chitosan and PVA was relatively different (Rc = 1.53 and RPVA = 1.35).

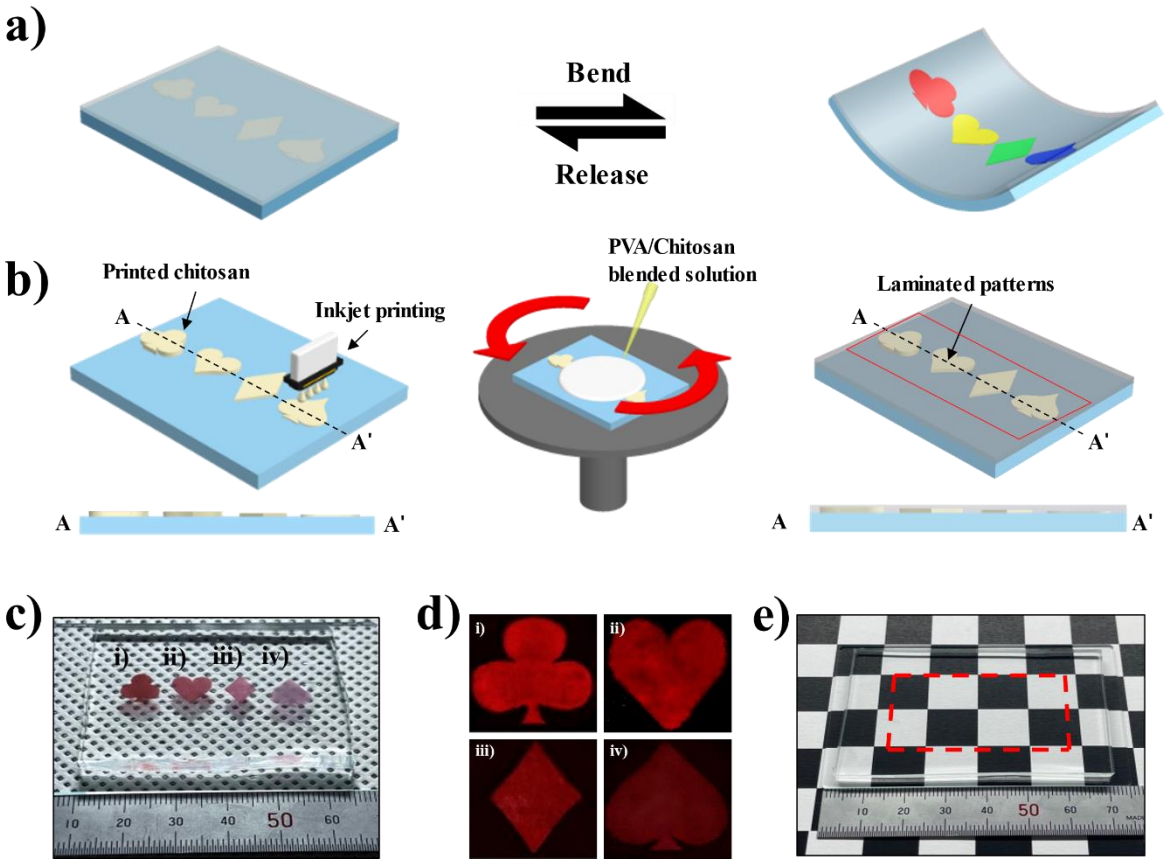

Figure 3-1. Concept and fabrication process of a trilayer thin film. (a) Schematic diagram of a flexible, transparent, and trilayered film that displays structural colors under external bending stresses. (b) Two-step fabrication processes for the trilayer film in which transparent patterns are formed, of which the material and geometrical properties are manipulated by inkjet printing. And then, the patterns are hidden by additionally spin-coating with PVA/chitosan solution. c) Optical image of a film device with different chitosan patterns before PVA/chitosan spin-coating. Because the chitosan solution/ink

was mixed with red food dye, the thicker the patterns the redder they are shown. d) Fluorescence images of the above patterns before PVA/chitosan spin-coating. The chitosan solution/ink was mixed with fluorescence dye (i.e., Rhodamine-B), the thicker the patterns are the stronger the fluorescence intensities are. e) Optical image of a flexible, transparent, and trilayered film after fully laminated by PVA/chitosan blending solution.

If the trilayered film is transparent in the natural state, it can well hide important information. Thus, to hide the chitosan interlayer pattern, the difference between the refractive index of the top layer and chitosan shall be less than 0.05. Thus, a mixture of PVA and chitosan was spin-coated to fully laminate the chitosan interlayer. The reasons for choosing a mixture of PVA and chitosan are as follows. First, the reflective index (R) of each thin film made of chitosan and PVA was relatively different (R_c = 1.53 and R_{PVA} = 1.35). For a thin film made of a mixture of PVA and chitosan, the resulting refractive index can be controlled linearly by adjusting their mixing ratio (v/v)[88], which is called a refractive index matching process[89] The reflective index of the thin film material made by a PVA and chitosan mixture in a 4:1 ratio was 1.49, which well met the aforementioned requirement. As shown in Figure 3-3, the top layer thickness can be easily realized by adjusting the spinning speed of the spin-coating.

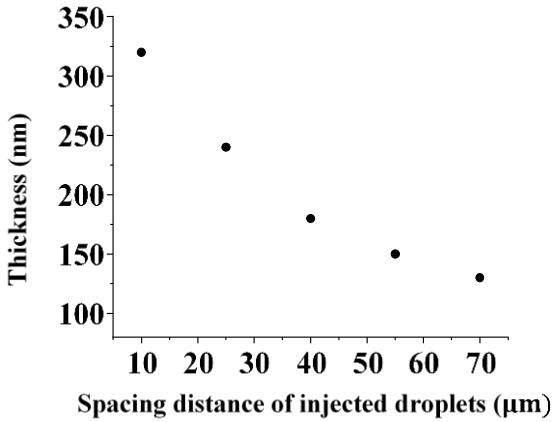

Figure 3-2. The relationship between the thickness of the chitosan interlayer pattern and the droplet spacing distance. The thickness of the inkjet-printed chitosan interlayer pattern decreases,

depending on the spacing distance of the injected droplets. In other words, the more the droplets are injected at the same pattern, the thicker the chitosan pattern is obtained

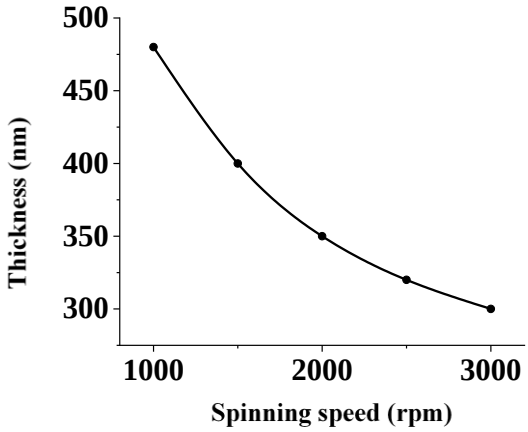

Figure 3-3. The relationship between the thickness of the top layer and the spinning speed for the top laminating layer. The thickness of the top layer is inversely proportional to the spinning speed. In other words, the top layer thickness made of a mixture of PVA and chitosan solution decreases as the spinning speed increases.

As shown in Figure 3-1e, the tri-layered film material obtained after covering the PVA/chitosan composite layer are still very transparent, and the pattern is well hidden. To further verify the refractive index matching approach, spectroscopy analysis was carried out by using UV-vis spectrometer as shown is Figure 3-4. The fabricated chitosan patterns/PDMS films shows a significant absorption in the visible light wavelength range. However, for the chitosan interlayers laminated with a PVA/chitosan composite, absorption is obviously weakened in the visible light wavelength range. Furthermore, to estimate the effect of printed chitosan interlayer on laminated film, we conducted a surface morphology analysis using an atomic force microscope (AFM). The AFM measurement results show that the surface roughness of the trilayer films ranges from 20 to 30 nm, which is very close to that of the bilayer films consisting of a top PVA/chitosan laminate and a PDMS substrate. This result demonstrated that the spin-coating of PVA/chitosan blending solution can fully laminate the

chitosan interlayer patterns on a PDMS substrate. The wrinkle formation mechanism was firstly established for a bilayer film. That is, a soft substrate with a thickness of 3 mm was used to generate uniform wrinkle structures (24).

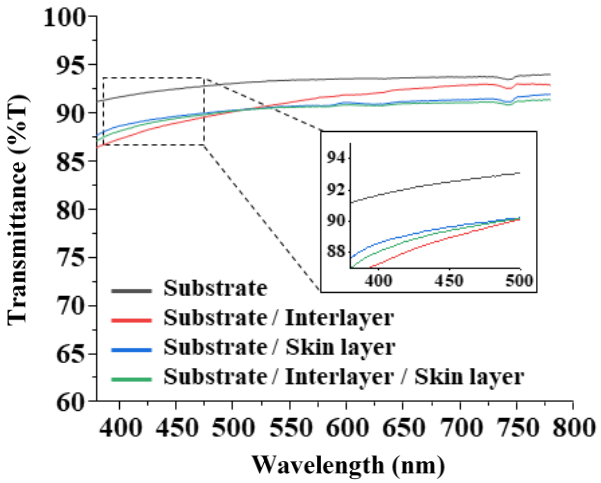

Figure 3-4. Transmittance spectra of the films used and fabricated. A spectroscopic investigation was conducted with four types of films: only substrate, the substrate with the chitosan interlayer, the substrate with the PVA/chitosan skin layer, and the final trilayer film. All the films show transparent characteristics in the visible light range.

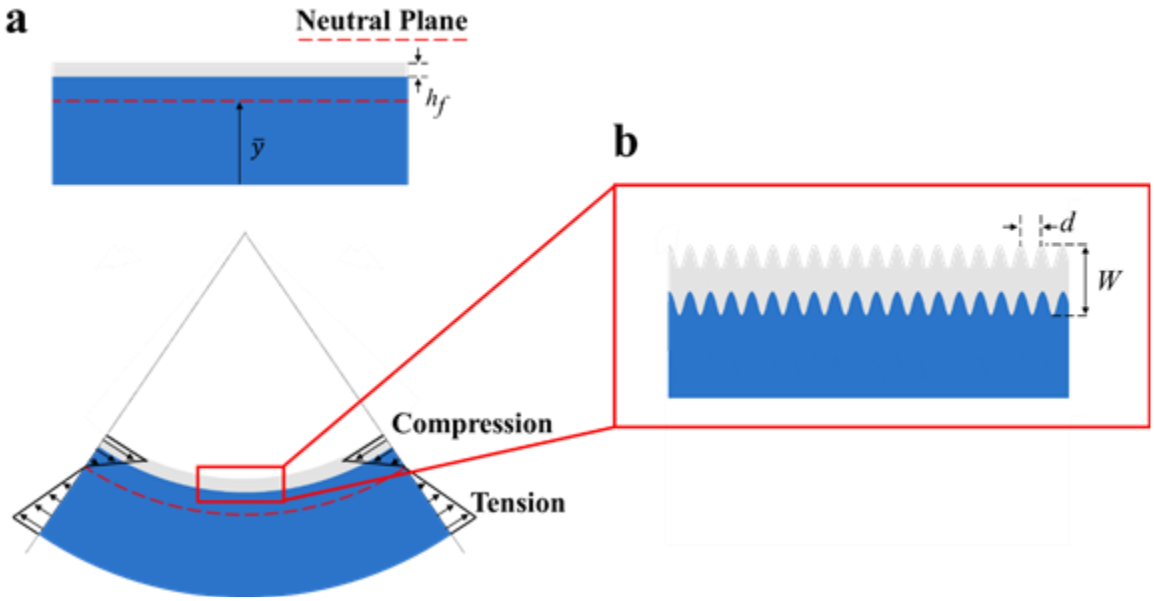

Figure 3-5. The wrinkle formation mechanism of the bilayer film. (a) Schematic of the cross-section view of the bilayer composite film device in the normal state (top, no stress) and the bended state

(bottom, compressive and tensile bending stresses). The dashed line in red indicates the neutral surface of stresses. (b) Schematic of the wrinkles generated at the top layer of the bilayer film.

For the bilayer film undergoing linear buckling as illustrated in Figure 3-5, a theoretical model has been well established and is described by the following equations (5):

$$l = 2\pi h_f \sqrt[3]{\frac{\overline{E}_f}{3\overline{E}_s}} = 2\pi h_f \sqrt[3]{\frac{E_f\,(1-\nu_s)}{3E_s\,(1-\nu_f)}} \tag{1}$$

$$W = h_f \sqrt{\frac{e_0}{e_c} - 1} \tag{2}$$

$$e_c = -\frac{1}{4}\sqrt[3]{\left(\frac{3\overline{E}_s}{\overline{E}_f}\right)^2} \tag{3}$$

where l, h_f, and W represent the wrinkle wavelength, the thickness of a stiff top layer, and the wrinkle amplitude, respectively. E_f and E_s represent the Young's moduli of the stiff top layer and the ductile bottom substrate, respectively. And, ν_f and ν_s represent the Poisson's ratios of the stiff top layer and the ductile bottom substrate, respectively. $\overline{E}$ represents the plane strain modulus, which is equivalent to $E(1-\nu)$; e_0 is the imposed strain and e_c is the critical strain of the wrinkles.

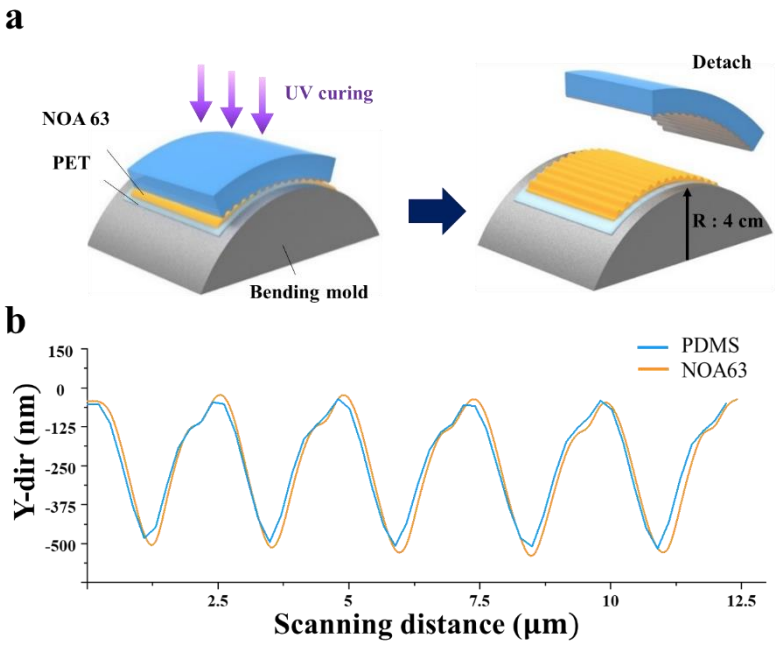

Figure 3-6. Wrinkle replication for precise characterization. a) Replication of the surface wrinkles generated on the trilayer film (top substrate) with the UV-curable and transparent adhesive NOA63 (bottom). The NOA63 on a PET substrate is very conformal to the nanoscale structures before UV-curing so that it precisely replicates the nanoscale wrinkles. After the UV-curing, the trilayer film was detached while leaving the replicated wrinkles on the adhesive NOA63 even after the replicated NOA63 substrate that was bended outward went back to the original flat state. b) Comparison of the replicated wrinkles by measuring the surface morphology of the NOA63 and the PDMS sample fabricated by using the NOA63 structure as a template mold. The profiles were measured by using an AFM.

Unidirectional deformation of the bilayer film by external mechanical stresses produces one-dimensional (1D) periodic wrinkles, which are well explained by the theoretical model. Note that the linear buckling instability occurs in the absence of the chitosan interlayer. Then, we investigated the formation of wrinkles of a bilayer film consisting of a stiff PVA/chitosan layer (E_f = 900 Mpa)[90] and a ductile PDMS substrate (E_f = 1.5 Mpa) apart from the role of chitosan interlayer. Because the Young's modulus of the PVA/chitosan composite film layer is followed by the composition ratio of chitosan and PVA which is significantly greater than that of PDMS. Inward bending with an 4 cm bending radius forms sinusoidal periodic wrinkles on the surface

of the PVA/chitosan composite layer. Since the wrinkle structure only appears in the bending state, it is not conducive to further characterizing its parameters using AFM. Thus, we replicated the surface wrinkle array of the bilayer film device on compression to a UV resin film on the PET substrate as shown in Figure S3-6a[91]. After curing, the bilayer film is detached while leaving the replicated wrinkles on the NOA63 even after the replicated NOA63 substrate is reversely bended back to be the original flat state. Therefore, PET sheets with the wrinkles on the surface can be analyzed directly with AFM, or used as templates to rub the wrinkle structure by PDMS for further analyses. As shown in Figure 3-6b, the wrinkle structure on PET surface and that on PDMS surface have very similar profiles, indicating the feasibility of this replication-based characterization method. Of course, the resulting wrinkles can be well explained by the 1D theoretical model aforementioned.

Figure 3-7a illustrates the wrinkle formation mechanism of a trilayer film to describe how various heterogenous wrinkles can be controlled by the chitosan interlayer pattern when the trilayer film was subjected to external mechanical stimuli. For a trilayer film as illustrated in Figure 3-7b, wrinkles can be defined using the linear buckling model which is explained by the following equations as suggested by Stafford[25]:

$$E_{\mathrm{eff}} = \frac{1+\mathrm{m}^2\mathrm{n}^4+2\mathrm{mn}(2\mathrm{n}^2+3\mathrm{n}+2)}{(1+\mathrm{n})^3(1+\mathrm{mn})}E_{\mathrm{i}} \tag{4}$$

$$\bar{y} = \frac{\left(\frac{t_{\mathrm{t}}}{2}\right)E_{\mathrm{t}}t_{\mathrm{t}}+\left(t_{\mathrm{t}}+\frac{t_{\mathrm{i}}}{2}\right)E_{\mathrm{i}}t_{\mathrm{i}}}{E_{\mathrm{t}}t_{\mathrm{t}}+E_{\mathrm{i}}t_{\mathrm{i}}} \tag{5}$$

where m is the ratio of Young's moduli of the top layer (E_{t}) and interlayer (E_{i}; i.e., $\mathrm{m} = E_{\mathrm{t}}/E_{\mathrm{i}}$), and n is the ratio of the top layer (t_{t}) and interlayer (t_{i}) thicknesses (i.e., $\mathrm{n} = t_{\mathrm{t}}/t_{\mathrm{i}}$). Additionally, the coordinate of the neutral plane from the bottom of the substrate ($\bar{y}$) was determined using the thickness of the interlayer. The wrinkles of the chitosan interlayer pattern region conformed to the Stafford model (i.e., Equation (4)), which defines the effective Young's modulus of the

two stiff layers attached to the bottom soft substrate. The vertical shift of the position of the neutral plane of the trilayer film makes it possible to tune the starting point of the instability position. Thus, in the presence of the chitosan interlayer pattern which is stiffer than the top laminated PVA/chitosan layer, the top surface above the chitosan pattern undergoes higher compressive stresses to form large amplitudes than the surrounding region that has no underlying chitosan pattern. These results further imply that the thickness of the chitosan interlayer pattern can control the wrinkle dimension locally; the thickness of the chitosan interlayer pattern can be simply adjusted by the inkjet printing method. Figure 3-7c shows the SEM images of various wrinkles generated by controlling the thickness of the interlayer patterns. We produced one bilayer film without the chitosan interlayer pattern and five trilayer films in which the chitosan interlayer pattern with the same shape but different thickness were printed individual. From the SEM images, we can see that the periodicity of the wrinkles varies and depends on the chitosan interlayer pattern. Figure 3-7d shows the quantified amplitude and wavelength (i.e., periodicity) of the wrinkles, which characterized the effect of the chitosan interlayer pattern on the resulting wrinkles in the trilayer film. In the case of the bilayer film (i.e., $t_i = 0$), the thickness of the top PVA/chitosan composite layer (h_f) was controlled to range from 480 nm to 300 nm, which was achieved by decreasing the spinning speed of the spin-coating process from 1000 rpm to 3000 rpm (Figure 3-8). As the h_f increased, the periodicity of the wrinkles also linearly increased from 410 nm to 950 nm. This result well matches with that estimated from Equation (1).

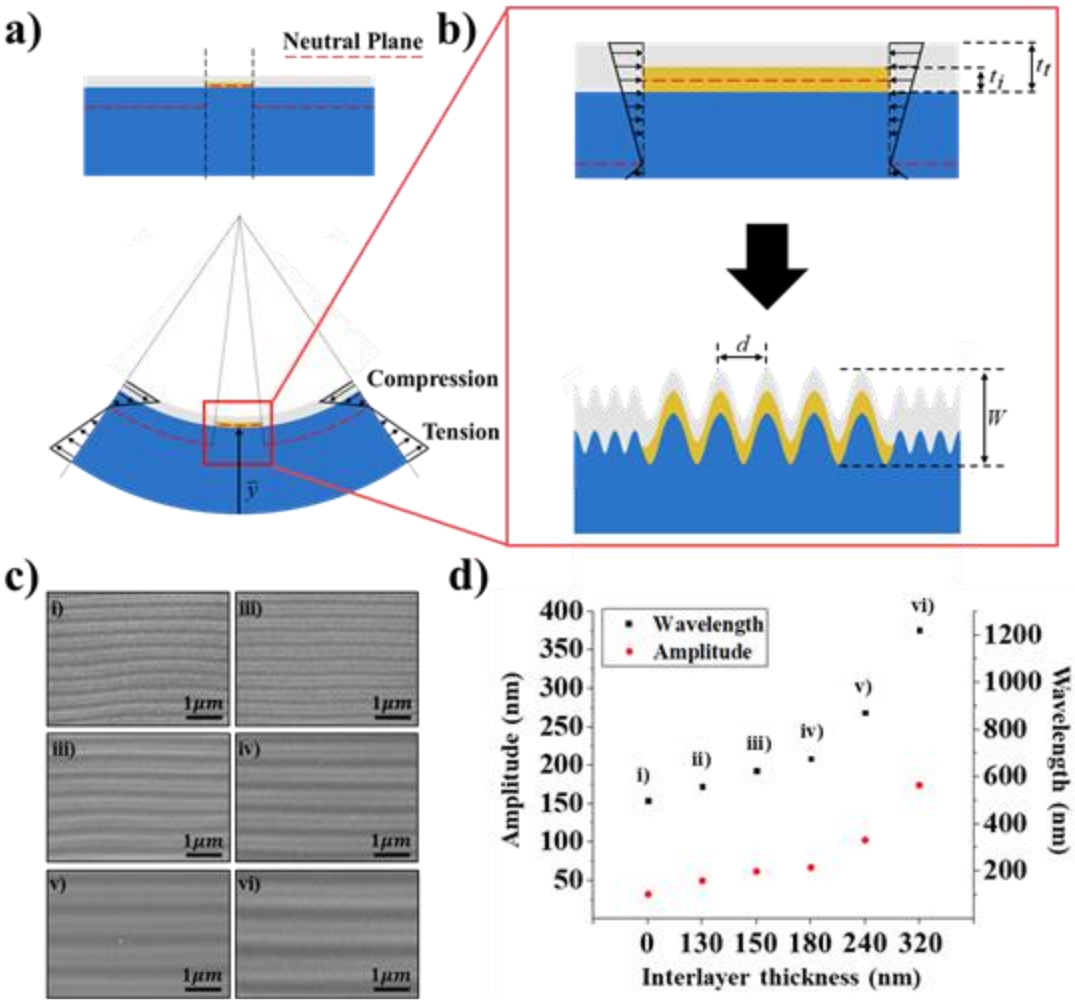

Figure 3-7. Basic mechanism of the wrinkle generation of the trilayer film. (a) Schematic of the cross-section view of the trilayer composite film device in the normal state (top, no stress) and the bended state (bottom, compressive and tensile bending stresses). The dashed line in red indicates the neutral surface of stresses. (b) Schematic of the patterned area out of the composite film device for which the neutral surface is shifted upward because of the discontinuous material property (top). When a bending stress is applied, wrinkles are formed, and their periodicities are governed by the resulting surface material properties as illustrated. (c) SEM images of various wrinkles of which periodicities (wavelength) are manipulated in tens of nanometers by controlling the chitosan interlayer thickness. (d) Amplitudes and wavelengths of the wrinkles measured by an AFM as the chitosan interlayer thickness increases.

On the other hand, the region with chitosan interlayer with various thicknesses ranging from 130 to 320 nm showed different wrinkle generation behavior. With 360 nm top layer thickness, the surface wrinkles are shown in scanning electron microscope (SEM) images (Figure 3-7c), show that wavelength of the surface wrinkles is going bigger as chitosan interlayer thickness increase. Furthermore, AFM results in Figure 2d shows that amplitude of surface wrinkles of the tri-layered film also increases as chitosan interlayer thickness increase (refer to Figure 3-8). For example, with a 130 nm chitosan interlayer height, the surface changes by external forces form wrinkles with a periodicity of 588 nm which slightly bigger than bilayer buckled surface. Eventually, a chitosan interlayer with a height of 320 nm results in wrinkles on laminated surface with a wavelength of about 1,250 nm. This is because the chitosan interlayer thickness increases means that the effective Young's modulus increases by Equation (4), the periodic wavelength changes followed by Equation (1). Meanwhile, in order to explain whether there is interaction between the area with interlayer and the area without interlayer, the microscopic morphology of the area is characterized. SEM images in Figure 3-9 show wrinkles near the boundary region separated by a chitosan-printed (patterned) region clearly. This laid the foundation for the presentation of complex patterns later.

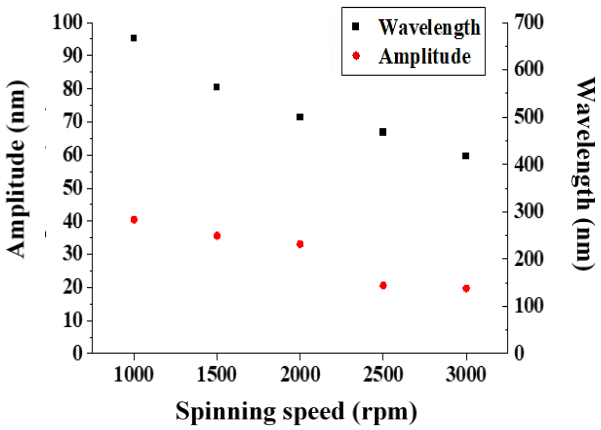

Figure 3-8. Effects of the PVA/chitosan top layer thickness on the resulting wrinkles for the bilayer films (with no chitosan interlayer). Both the amplitude and the wavelength of the wrinkles decrease as the thickness of the PVA/chitosan top layer decreases (i.e., as the spinning speed for spin-coating increases). All the measurement was conducted by AFM in the absence of the chitosan interlayer pattern.

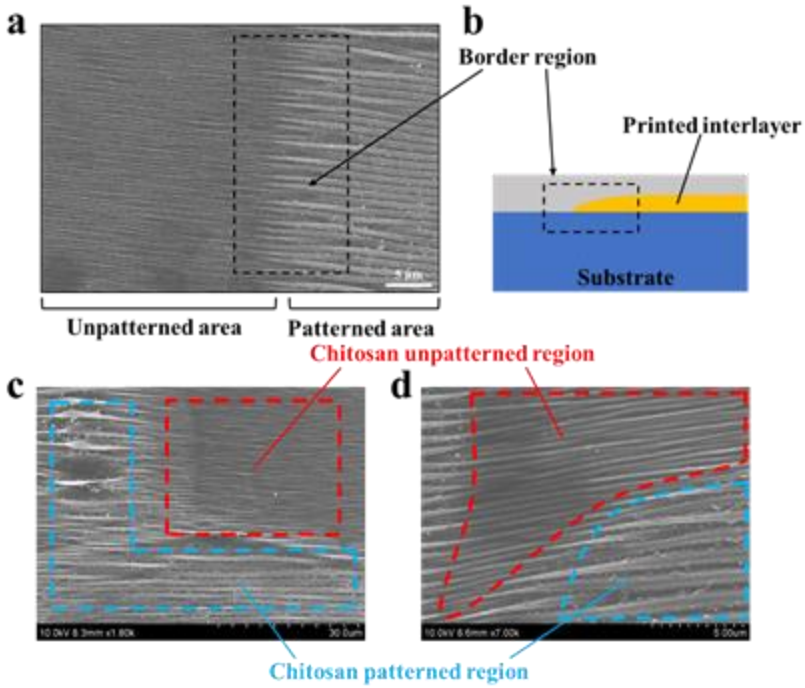

Figure 3-9. The SEM images **show wrinkles near the boundary region separated by a chitosan-printed (patterned) region.** a) SEM image shows two different types of wrinkles with short (unpatterned region) and long (patterned) wavelengths, respectively. b) Illustration of the cross-section of a chitosan-printed pattern that is covered with another PVA/chitosan layer (top). c)–d) Zoomed SEM images clearly show two types of wrinkles that are manipulated by selectively printing chitosan solution where a pattern is generated.

Figure 3-10 shows the optical characterization results of three different structural colors generated by controlling the wrinkles according to the theoretical model of the trilayer film. First, as shown in Figure 3-11a, when the laminated trilayer composite film was bended in the inward direction, the periodic wrinkle structures show diverse colors in response to the incident light. The optical characteristics of the mechanochromic responses of the three trilayer films were different; the central spade patterns show different color spectra (blue, green, and red)

although almost the same external mechanical force was imposed on. This is due to the controllable periodicity of tens of nm of the wrinkles of which the interference with incident light makes it possible to emit different colors from blue to red.

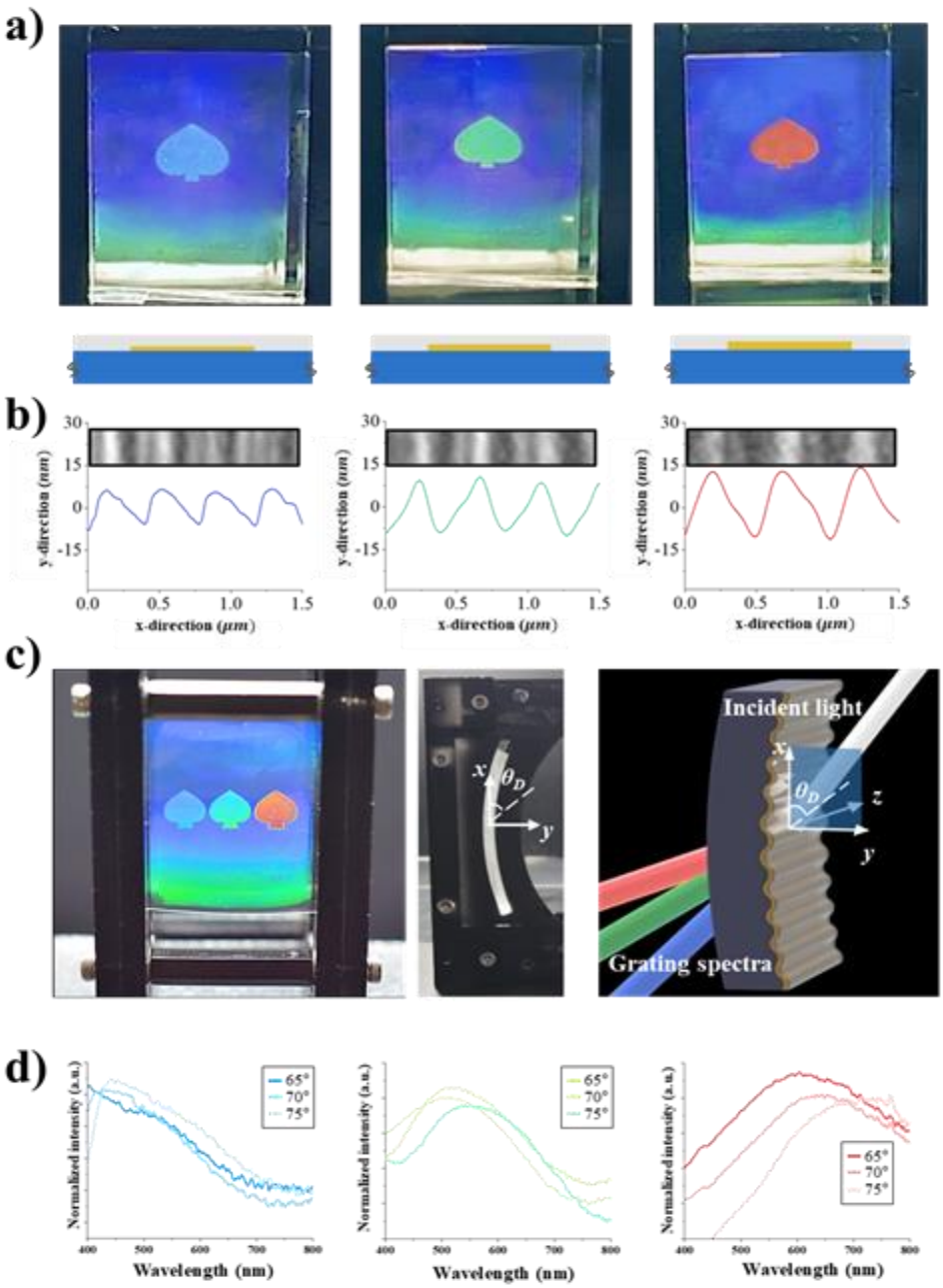

Figure 3-10. Generation of multi-modal structural colors and their optical and structural characterization. (a) Three representative structural colors were displayed by manipulating the thickness of the chitosan interlayer pattern (i.e., spade). This was possible by creating three different wrinkle periodicities separately. (b) The height and width of the wrinkles measured by AFM, and SEM

image of the corresponding wrinkles in the same order as above. (c) Three different structural colors are simultaneously displayed by a single trilayer film device inward bended. This was possible by adjusting the chitosan interlayer thickness during inkjet printing. Schematic diagram of the optical ray paths propagating through the trilayer film. (d) Spectrum shifts were quantitatively characterized and depended on the viewing angles and the wrinkle periodicities.

Mechanical deformation may induce structural colors because the periodic wrinkles are formed on the surface and act as the diffraction grating. We further investigated the optical property of the precisely controlled multiple wrinkles based on different chitosan interlayer thickness as shown in Figure 3-11b (e.g., t_i = 588 nm for blue , t_i = 625 nm for green, and t_i = 667 nm for red). Figure 3-10c shows a trilayer film in which several printing areas were segmented and fabricated by printing three different chitosan interlayer patterns simultaneously on one film device, which shows multicolor patterns at a time. The blue, green, and red spade patterns were produced by modulating the thickness of the chitosan interlayer patterns in the same manner as those in Figure 3-10a. The structural coloration mechanism can be derived from the path difference of the incident light through the wrinkle grating; the wavelength of the incident light ranged from 400 nm to 800 nm. The iridescent color variation can be explained by the constructive interference of the light with various wrinkle gratings; that is, the theoretical diffraction equation is $n\lambda_w = d(\sin\theta_D - \sin\theta_I)$ where the integer n is the order of diffraction, λ_w is the wavelength of white light, d is the wavelength of wrinkles, θ_D and θ_I are the observation and incidence angle, respectably.[68] It can be seen from the above formula that when the value of d is relatively large, the wavelength range of the observed light is wider[92]. This also explains that the surrounding area with no interlayer pattern is basically blue regardless of the central spade patterns while the central spade patterns with a chitosan interlayer beneath show a spectral shift from blue to red according to the different intermediate layer properties. At the same time, according to Equation (4), due to the shift of the neutral

plane, the stronger compressive stresses are imposed on the patterned region with the chitosan interlayer beneath. Therefore, according to Equation (1), the amplitude of this part is also bigger. Because the diffraction efficiency depends on the amplitude, the higher the amplitude of wrinkles is generated, the clearer colors are displayed[84]. Therefore, the trilayer film structure is very useful and necessary.

We further systemically analyzed the mechanochromic color response to the viewing angle. Figure 3-10d shows various diffraction peaks in response to the different viewing angles varying from 65˚ to 75˚. For the blue spade pattern, as the viewing angle increases, the diffraction peaks shifted from 420 nm to 450 nm. It shows a quasi-linear dependence on the viewing angle. This dependence became more prominent with the increasing wrinkle periodicity (from the blue to the red spade pattern). For the red pattern on the right, as the viewing angle increased, their diffraction peaks were observed at approximately 570 nm and 630 nm, respectively, and the difference in the angle dependence of the diffraction peaks was even higher than that of the blue. Therefore, we demonstrated that a single transparent trilayer film makes it possible to display multi-modal, holographic, and colorful images, showina a remarkable potential for the various optical, mechanochromic applicability. Note that this ability can be largely attributed to the material-property patterning technique.

Figure 3-11 shows several practical applications of the covert-overt, multi-holographic, and multi-modal trilayer composite film. Figure 3-11a shows a dual trilayer composite film that was obtained by bonding two pieces of trilayer films with the patterns outside. It remains transparent in the absence of external stimuli. When bending in different directions, either the flower pattern or the old palace pattern was displayed selectively and independently. Careful observation of details reveals that both the patterns have three color segmentations/distributions. The right flower-patterned device shows three distinct colors such as left and right petals, and

branches). Similarly, the left complex pattern of the old palace pattern consists of three vertical segments, and each segment shows different colors. This is because each pattern was fabricated to form nanoscale wrinkles with different wavelengths by adjusting the thickness of the chitosan interlayer. Note that the inkjet printing method can directly control the color of the segmented areas even for complex patterns and the wrinkles generated in the different segments do not interfere with each other.

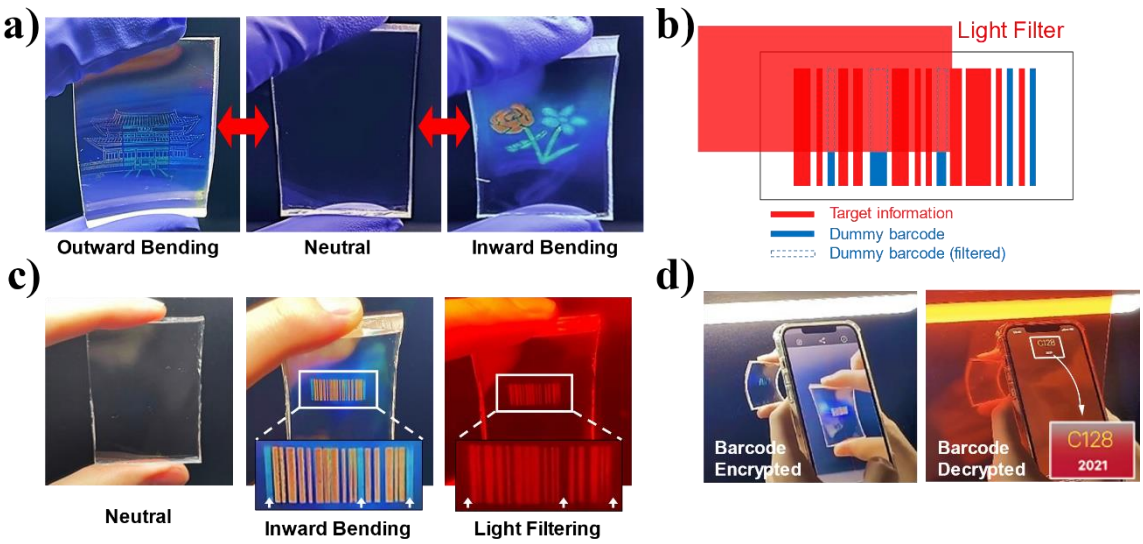

Figure 3-11. Application of the multi-holographic and multi-modal display trilayer film devices to anticounterfeiting techniques. (a) Two trilayer films are bonded with the patterns outside. Optical images of the films are shown when outward bending, neutral, and inward bending state, respectively. Both the patterns consist of three segments, which independently display their own distinct structural colors because each segment was fabricated to have different chitosan interlayer thicknesses. (b) Demonstration of a novel decoding process for a multi-colored barcode system. (c) Optical images of a trilayer film device and demonstration of the developed new barcode system. (d) Demonstration of the encryption (left) and description (right) process using a color filter. The correct information from the new barcode system is executed via a mobile phone.

Finally, we demonstrated a new, multi-color-based barcode system by developing a novel decoding process using a light filter. As shown in Figure 3-11b, we demonstrated that the multi-modal trilayer film can embed barcode information into colors. The barcodes consisted of red

target information and blue dummy one. They were initially covert and encrypted but they turned out to be overt when bended. However, a red light filter was necessary to retrieve only correct barcodes. Figure 3-11c shows a real trilayer film device that was initially transparent but the hidden barcodes were vividly shown by bending the device with fingers. As previously mentioned, only target barcode information was decoded by applying a red light filter to the device as shown. Figure 4d further demonstrated information decryption process using a smart phone. It can be seen more clearly from the Supplementary Movie S1, under compression, the multi-color embedded barcodes cannot be identified by the smartphone application because the barcodes were intentionally protected by arbitrary dummy barcodes with specific colors. These characteristics made it difficult to identify the barcode information. However, it was successfully to decrypt the barcode information correctly by employing a light filter and using a commercial barcode reader app.

3.4 Conclusions

In this study, we developed a transparent, flexible composite film consisting of a ductile top, a ductile bottom layer, and a stiff interlayer. A lastic substrate was used for the bottom layer such as PDMS. The interlayer was fabricated by using an inkjet printer that can produce various patterns on top of the bottom layer. And then, the top layer was spin-coated with a solution to not only protect the patterns but also generate local wrinkles in a selective manner. We demonstrate that the nanoscale controlling of wrinkles caused by external stimuli through the patterning of material properties with a novel and simple approach. A trilayer film with different mechanical properties was produced by inkjet printing. The volume fraction ratio of the chitosan interlayer to the laminated PVA/chitosan composite and the multi-scale wrinkles caused by external mechanical stimulus were obtained depending on the patterned material property. The periodicity of the wrinkles could be controlled to tens of nanometers, allowing the color adjustment of visible light in certain planes. This allowed mixed color and cascaded color combinations through mechanochromic response by external stimuli. We also demonstrated an enhanced anti-counterfeiting film through a new type of barcode that can hide information in colors. These advantages offer the potential for next-generation wrinkle-based smart optical systems.

Chapter 4 Conclusion and future perspective

Using the development of inkjet printing process technology, this dissertation introduced a method of manufacturing micro/nanostructures on a substrate and laminating them inside a film. By adjusting the refractive index of the laminate material and the pattern structure, it was possible to hide the structure while maintaining perfect transparency in the basic state. In addition, the laminated structure selectively changed the material properties of the surface, thus securing the controllability of the model and geometry. According to the traditional buckling theory, wrinkles were formed in heterogeneous or multi-types due to the instability effect according to mechanical material properties, and it was confirmed that they act as excellent photonic crystal materials.

As a result, laminated film using two kinds of materials with similar optical properties and different mechanical properties can provide the following advantages.

1) The color expression of the pattern can be made semi-permanent by causing scattering with external light using transformable nanostructures rather than general dyes.

2) In the transparent state, it can be completely hidden (covert), and when an external force is applied, it can induce a quick cognitive response (overt) of the user by immediately expressing natural color.

3) It is possible to express high-resolution natural colors with only finger strength and without external devices (light, heat).

Therefore, the expandability and feasibility of the application of the developed device was clearly demonstrated. In addition, future perspectives of the device developed in this dissertation include further development and efforts, such as the development of base technology for large-area and the efficient production of bi- and trilayer films via a one-step process for technology transfer and commercialization.

Reference

1. Yoshioka, S.; Kinoshita, S., Wavelength–selective and anisotropic light–diffusing scale on the wing of the Morpho butterfly. *Proceedings of the Royal Society of London. Series B: Biological Sciences* **2004,** *271* (1539), 581-587.

2. Gaillou, E.; Fritsch, E.; Aguilar-Reyes, B.; Rondeau, B.; Post, J.; Barreau, A.; Ostroumov, M., Common gem opal: An investigation of micro-to nano-structure. *American Mineralogist* **2008,** *93* (11-12), 1865-1873.

3. Liu, F.; Dong, B.; Liu, X.; Zheng, Y.; Zi, J., Structural color change in longhorn beetles Tmesisternus isabellae. *Optics express* **2009,** *17* (18), 16183-16191.

4. Lee, G. H.; Choi, T. M.; Kim, B.; Han, S. H.; Lee, J. M.; Kim, S.-H., Chameleon-inspired mechanochromic photonic films composed of non-close-packed colloidal arrays. *ACS nano* **2017,** *11* (11), 11350-11357.

5. Vigneron, J. P.; Pasteels, J. M.; Windsor, D. M.; Vértesy, Z.; Rassart, M.; Seldrum, T.; Dumont, J.; Deparis, O.; Lousse, V.; Biro, L. P., Switchable reflector in the Panamanian tortoise beetle Charidotella egregia (Chrysomelidae: Cassidinae). *Physical Review E* **2007,** *76* (3), 031907.

6. Stan, C. V.; Beavers, C. M.; Kunz, M.; Tamura, N., X-ray diffraction under extreme conditions at the Advanced Light Source. *Quantum Beam Science* **2018,** *2* (1), 4.

7. Matsuo, S.; Shinya, A.; Kakitsuka, T.; Nozaki, K.; Segawa, T.; Sato, T.; Kawaguchi, Y.; Notomi, M., High-speed ultracompact buried heterostructure photonic-crystal laser with 13 fJ of energy consumed per bit transmitted. *Nature Photonics* **2010,** *4* (9), 648-654.

8. Chen, H.; Lou, R.; Chen, Y.; Chen, L.; Lu, J.; Dong, Q., Photonic crystal materials and their application in biomedicine. *Drug Delivery* **2017,** *24* (1), 775-780.

9. Liu, H.; Li, Z.; Shen, R.; Li, Z.; Yang, Y.; Yuan, Q., Point-of-care pathogen testing using photonic crystals and machine vision for diagnosis of urinary tract infections. *Nano Letters* **2021,** *21* (7), 2854-2860.

10. Lim, H. S.; Lee, J.-H.; Walish, J. J.; Thomas, E. L., Dynamic swelling of tunable full-color block copolymer photonic gels via counterion exchange. *ACS nano* **2012,** *6* (10), 8933-8939.

11. Rommel, M.; Spolidi, G.; Yanev, V., J. Vac. Sci. Technol., B: Nanotechnol. Microelectron.: Mater., Process., Meas. *Phenom.* **2010,** *28*, 595.

12. Gao, Y.; Huang, C.; Hao, C.; Sun, S.; Zhang, L.; Zhang, C.; Duan, Z.; Wang, K.; Jin, Z.; Zhang, N., Lead halide perovskite nanostructures for dynamic color display. *ACS nano* **2018,** *12* (9), 8847-8854.

13. Wang, H.; Haroldson, R.; Balachandran, B.; Zakhidov, A.; Sohal, S.; Chan, J. Y.; Zakhidov, A.; Hu, W., Nanoimprinted perovskite nanograting photodetector with improved efficiency. *ACS nano* **2016,** *10* (12), 10921-10928.

14. Armstrong, E.; Khunsin, W.; Osiak, M.; Blömker, M.; Torres, C. M. S.; O'Dwyer, C., Ordered 2D colloidal photonic crystals on gold substrates by surfactant-assisted fast-rate dip coating. *Small* **2014,** *10* (10), 1895-1901.

15. Yang, H.; Jiang, P., Large-scale colloidal self-assembly by doctor blade coating. *Langmuir* **2010,** *26* (16), 13173-13182.

16. Nam, H.; Song, K.; Ha, D.; Kim, T., Inkjet printing based mono-layered photonic crystal patterning for anti-counterfeiting structural colors. *Scientific reports* **2016,** *6* (1), 1-9.

17. Ogi, T.; Modesto-Lopez, L. B.; Iskandar, F.; Okuyama, K., Fabrication of a large

area monolayer of silica particles on a sapphire substrate by a spin coating method. *Colloids and Surfaces A: Physicochemical and Engineering Aspects* **2007,** *297* (1-3), 71-78.

18. Han, M. G.; Shin, C. G.; Jeon, S. J.; Shim, H.; Heo, C. J.; Jin, H.; Kim, J. W.; Lee, S., Full color tunable photonic crystal from crystalline colloidal arrays with an engineered photonic stop-band. *Advanced Materials* **2012,** *24* (48), 6438-6444.

19. Mapas, J. K. D.; Thomay, T.; Cartwright, A. N.; Ilavsky, J.; Rzayev, J., Ultrahigh molecular weight linear block copolymers: Rapid access by reversible-deactivation radical polymerization and self-assembly into large domain nanostructures. *Macromolecules* **2016,** *49* (10), 3733-3738.

20. Fudouzi, H.; Xia, Y., Photonic papers and inks: color writing with colorless materials. *Advanced Materials* **2003,** *15* (11), 892-896.

21. Zhang, Z.; Chen, Z.; Wang, Y.; Chi, J.; Wang, Y.; Zhao, Y., Bioinspired bilayer structural color hydrogel actuator with multienvironment responsiveness and survivability. *Small Methods* **2019,** *3* (12), 1900519.

22. Ge, J.; Kwon, S.; Yin, Y., Niche applications of magnetically responsive photonic structures. *Journal of Materials Chemistry* **2010,** *20* (28), 5777-5784.

23. Jia, L.; Li, M.; Jiang, L.; Gao, H.; Tan, H.; Peng, B.; Xu, J.; Zhang, L.; Zhu, J., Revealable photonic prints with oppositely responsive polymers for improved visual sensing. *Journal of Materials Chemistry C* **2020,** *8* (27), 9286-9292.

24. Xuan, R.; Wu, Q.; Yin, Y.; Ge, J., Magnetically assembled photonic crystal film for humidity sensing. *Journal of Materials Chemistry* **2011,** *21* (11), 3672-3676.

25. Xu, H.; Yu, C.; Wang, S.; Malyarchuk, V.; Xie, T.; Rogers, J. A., Deformable, programmable, and shape-memorizing micro-optics. *Advanced Functional Materials* **2013,** *23* (26), 3299-3306.

26. Ge, D.; Lee, E.; Yang, L.; Cho, Y.; Li, M.; Gianola, D. S.; Yang, S., A robust smart window: reversibly switching from high transparency to angle-independent structural color display. *Advanced Materials* **2015,** *27* (15), 2489-2495.

27. Li, Z.; Liu, Y.; Marin, M.; Yin, Y., Thickness-dependent wrinkling of PDMS films for programmable mechanochromic responses. *Nano Research* **2020**, 1-7.

28.Fu, X.; Peng, C.; Samal, M.; Barange, N.; Chen, Y.-A.; Shin, D.-H.; Mehta, Y.; Rozelle, A.; Chang, C.-H.; So, F., Mode Dispersion in Photonic Crystal Organic Light-Emitting Diodes. *ACS Applied Electronic Materials* **2020,** *2* (6), 1759-1767.

29. Fan, W.; Zeng, J.; Gan, Q.; Ji, D.; Song, H.; Liu, W.; Shi, L.; Wu, L., Iridescence-controlled and flexibly tunable retroreflective structural color film for smart displays. *Science advances* **2019,** *5* (8), eaaw8755.

30. Huo, P.; Song, M.; Zhu, W.; Zhang, C.; Chen, L.; Lezec, H. J.; Lu, Y.; Agrawal, A.; Xu, T., Photorealistic full-color nanopainting enabled by a low-loss metasurface. *Optica* **2020,** *7* (9), 1171-1172.

31. Li, Q.; Liu, S.; Wang, J.; Mbola, N. M.; Meng, Z.; Wang, X.; Xue, M., A biocompatible, self-adhesive, and stretchable photonic crystal sensor for underwater motion detection. *Journal of Materials Chemistry C* **2022,** *10* (23), 9025-9034.

32. Maeng, B.; Chang, H.-k.; Park, J., Photonic crystal-based smart contact lens for continuous intraocular pressure monitoring. *Lab on a Chip* **2020,** *20* (10), 1740-1750.

33. Yetisen, A. K.; Butt, H.; da Cruz Vasconcellos, F.; Montelongo, Y.; Davidson, C. A.; Blyth, J.; Chan, L.; Carmody, J. B.; Vignolini, S.; Steiner, U., Light-directed writing of chemically tunable narrow-band holographic sensors. *Advanced Optical Materials* **2014,** *2* (3), 250-254.

34. Viswanathan, S.; Narayanan, T. N.; Aran, K.; Fink, K. D.; Paredes, J.; Ajayan,

P. M.; Filipek, S.; Miszta, P.; Tekin, H. C.; Inci, F., Graphene–protein field effect biosensors: glucose sensing. *Materials Today* **2015,** *18* (9), 513-522.

35. Yetisen, A. K.; Montelongo, Y.; da Cruz Vasconcellos, F.; Martinez-Hurtado, J.; Neupane, S.; Butt, H.; Qasim, M. M.; Blyth, J.; Burling, K.; Carmody, J. B., Reusable, robust, and accurate laser-generated photonic nanosensor. *Nano letters* **2014,** *14* (6), 3587-3593.

36. Shafiee, H.; Lidstone, E. A.; Jahangir, M.; Inci, F.; Hanhauser, E.; Henrich, T. J.; Kuritzkes, D. R.; Cunningham, B. T.; Demirci, U., Nanostructured optical photonic crystal biosensor for HIV viral load measurement. *Scientific reports* **2014,** *4* (1), 1-7.

37. Arppe, R.; Sørensen, T. J., Physical unclonable functions generated through chemical methods for anti-counterfeiting. *Nature Reviews Chemistry* **2017,** *1* (4), 1-13.

38. Meng, Y.; Qiu, J.; Wu, S.; Ju, B.; Zhang, S.; Tang, B., Biomimetic structural color films with a bilayer inverse heterostructure for anticounterfeiting applications. *ACS applied materials & interfaces* **2018,** *10* (44), 38459-38465.

39. Hou, J.; Zhang, H.; Su, B.; Li, M.; Yang, Q.; Jiang, L.; Song, Y., Four-Dimensional Screening Anti-Counterfeiting Pattern by Inkjet Printed Photonic Crystals. *Chemistry–An Asian Journal* **2016,** *11* (19), 2680-2685.

40. Li, Y.; Zhou, X.; Yang, Q.; Li, Y.; Li, W.; Li, H.; Chen, S.; Li, M.; Song, Y., Patterned photonic crystals for hiding information. *Journal of Materials Chemistry C* **2017,** *5* (19), 4621-4628.

41. Tan, H.; Lyu, Q.; Xie, Z.; Li, M.; Wang, K.; Wang, K.; Xiong, B.; Zhang, L.; Zhu, J., Metallosupramolecular Photonic Elastomers with Self-Healing Capability and Angle-Independent Color. *Advanced Materials* **2019,** *31* (6), 1805496.

42. Liu, C.; Ding, H.; Wu, Z.; Gao, B.; Fu, F.; Shang, L.; Gu, Z.; Zhao, Y., Tunable Structural Color Surfaces with Visually Self-Reporting Wettability. *Advanced Functional Materials* **2016,** *26* (43), 7937-7942.

43. Shang, Y.; Chen, Z.; Fu, F.; Sun, L.; Shao, C.; Jin, W.; Liu, H.; Zhao, Y., Cardiomyocyte-driven structural color actuation in anisotropic inverse opals. *Acs Nano* **2018,** *13* (1), 796-802.

44. Chen, Z.; Fu, F.; Yu, Y.; Wang, H.; Shang, Y.; Zhao, Y., Cardiomyocytes-Actuated Morpho Butterfly Wings. *Advanced Materials* **2019,** *31* (8), 1805431.

45. Ohtsuka, Y.; Seki, T.; Takeoka, Y., Thermally tunable hydrogels displaying angle-independent structural colors. *Angewandte Chemie* **2015,** *127* (51), 15588-15593.

46. Chang, H.-K.; Chang, G. T.; Thokchom, A. K.; Kim, T.; Park, J., Ultra-fast responsive colloidal–polymer composite-based volatile organic compounds (VOC) sensor using nanoscale easy tear process. *Scientific reports* **2018,** *8* (1), 1-11.

47. Nucara, L.; Greco, F.; Mattoli, V., Electrically responsive photonic crystals: a review. *Journal of Materials Chemistry C* **2015,** *3* (33), 8449-8467.

48. Wang, W.; Fan, X.; Li, F.; Qiu, J.; Umair, M. M.; Ren, W.; Ju, B.; Zhang, S.; Tang, B., Magnetochromic photonic hydrogel for an alternating magnetic field-responsive color display. *Advanced Optical Materials* **2018,** *6* (4), 1701093.

49. Park, T. H.; Yu, S.; Cho, S. H.; Kang, H. S.; Kim, Y.; Kim, M. J.; Eoh, H.; Park, C.; Jeong, B.; Lee, S. W., Block copolymer structural color strain sensor. *NPG Asia Materials* **2018,** *10* (4), 328-339.

50. Cai, Z.; Kwak, D. H.; Punihaole, D.; Hong, Z.; Velankar, S. S.; Liu, X.; Asher, S. A., A photonic crystal protein hydrogel sensor for Candida albicans. *Angewandte Chemie* **2015,** *127* (44), 13228-13232.

51. Fu, F.; Shang, L.; Chen, Z.; Yu, Y.; Zhao, Y., Bioinspired living structural color hydrogels. *Science Robotics* **2018,** *3* (16), eaar8580.

52. Kim, H. N.; Yang, S., Responsive smart windows from nanoparticle–polymer composites. *Advanced Functional Materials* **2020,** *30* (2), 1902597.

53. Zhao, Z.; Wang, H.; Shang, L.; Yu, Y.; Fu, F.; Zhao, Y.; Gu, Z., Bioinspired heterogeneous structural color stripes from capillaries. *Advanced Materials* **2017,** *29* (46), 1704569.

54. Fang, Y.; Ni, Y.; Leo, S.-Y.; Taylor, C.; Basile, V.; Jiang, P., Reconfigurable photonic crystals enabled by pressure-responsive shape-memory polymers. *Nature communications* **2015,** *6* (1), 1-8.

55. Zhang, G.; Peng, W.; Wu, J.; Zhao, Q.; Xie, T., Digital coding of mechanical stress in a dynamic covalent shape memory polymer network. *Nature communications* **2018,** *9* (1), 1-7.

56. Choi, W. S.; Kim, M.; Park, S.; Lee, S. K.; Kim, T., Patterning and transferring hydrogel-encapsulated bacterial cells for quantitative analysis of synthetically engineered genetic circuits. *Biomaterials* **2012,** *33* (2), 624-633.

57. Zhou, Q.; Park, J. G.; Kim, K. N.; Thokchom, A. K.; Bae, J.; Baik, J. M.; Kim, T., Transparent-flexible-multimodal triboelectric nanogenerators for mechanical energy harvesting and self-powered sensor applications. *Nano Energy* **2018,** *48*, 471-480.

58. Khlebtsov, B. N.; Khanadeev, V. A.; Khlebtsov, N. G., Determination of the size, concentration, and refractive index of silica nanoparticles from turbidity spectra. *Langmuir* **2008,** *24* (16), 8964-8970.

59. Cardenas-Valencia, A. M.; Dlutowski, J.; Fries, D.; Langebrake, L., Spectrometric determination of the refractive index of optical wave guiding materials used in lab-on-a-chip applications. *Applied spectroscopy* **2006,** *60* (3), 322-329.

60. Hsiung, B.-K.; Siddique, R. H.; Stavenga, D. G.; Otto, J. C.; Allen, M. C.; Liu, Y.; Lu, Y.-F.; Deheyn, D. D.; Shawkey, M. D.; Blackledge, T. A., Rainbow peacock spiders inspire miniature super-iridescent optics. *Nature communications* **2017,** *8* (1), 1-8.

61. Fernandes, S. N.; Geng, Y.; Vignolini, S.; Glover, B. J.; Trindade, A. C.; Canejo, J. P.; Almeida, P. L.; Brogueira, P.; Godinho, M. H., Structural color and iridescence in transparent sheared cellulosic films. *Macromolecular Chemistry and Physics* **2013,** *214* (1), 25-32.

62. Viel, B.; Ruhl, T.; Hellmann, G. P., Reversible deformation of opal elastomers. *Chemistry of Materials* **2007,** *19* (23), 5673-5679.

63. Thokchom, A. K.; Zhou, Q.; Kim, D.-J.; Ha, D.; Kim, T., Characterizing self-assembly and deposition behavior of nanoparticles in inkjet-printed evaporating droplets. *Sensors and Actuators B: Chemical* **2017,** *252*, 1063-1070.

64. Chung, J. Y.; Nolte, A. J.; Stafford, C. M., Surface wrinkling: a versatile platform for measuring thin-film properties. *Advanced materials* **2011,** *23* (3), 349-368.

65. Xie, T.; Xiao, X.; Li, J.; Wang, R., Encoding localized strain history through wrinkle based structural colors. *Advanced Materials* **2010,** *22* (39), 4390-4394.

66. Yang, S.; Khare, K.; Lin, P. C., Harnessing surface wrinkle patterns in soft matter. *Advanced Functional Materials* **2010,** *20* (16), 2550-2564.

67. Wu, H.; Jiao, Y.; Zhang, C.; Chen, C.; Yang, L.; Li, J.; Ni, J.; Zhang, Y.; Li, C.; Zhang, Y., Large area metal micro-/nano-groove arrays with both structural color and anisotropic wetting fabricated by one-step focused laser interference lithography. *Nanoscale* **2019,** *11* (11), 4803-4810.

68. Whitney, H. M.; Kolle, M.; Andrew, P.; Chittka, L.; Steiner, U.; Glover, B. J., Floral iridescence, produced by diffractive optics, acts as a cue for animal pollinators. *Science* **2009,** *323* (5910), 130-133.

69. Al-Otum, H.; Al-Shalabi, N. E., Copyright protection of color images for android-based smartphones using watermarking with quick-response code. *Multimedia Tools and Applications* **2018,** *77* (12), 15625-15655.

70. Bowden, N.; Brittain, S.; Evans, A. G.; Hutchinson, J. W.; Whitesides, G. M., Spontaneous formation of ordered structures in thin films of metals supported on an elastomeric polymer. *Nature* **1998,** *393* (6681), 146-149.

71. Harrison, C.; Stafford, C. M.; Zhang, W.; Karim, A., Sinusoidal phase grating created by a tunably buckled surface. *Applied Physics Letters* **2004,** *85* (18), 4016-4018.

72. Khang, D.-Y.; Jiang, H.; Huang, Y.; Rogers, J. A., A stretchable form of single-crystal silicon for high-performance electronics on rubber substrates. *Science* **2006,** *311* (5758), 208-212.

73. Strübing, T.; Khosravanizadeh, A.; Vilfan, A.; Bodenschatz, E.; Golestanian, R.; Guido, I., Wrinkling instability in 3D active nematics. *Nano letters* **2020,** *20* (9), 6281-6288.

74. Melzer, M.; Karnaushenko, D.; Lin, G.; Baunack, S.; Makarov, D.; Schmidt, O. G., Direct transfer of magnetic sensor devices to elastomeric supports for stretchable electronics. *Advanced Materials* **2015,** *27* (8), 1333-1338.

75. Qi, H.; Wang, S.; Li, C.; Zhao, Y.; Xu, B.; Jiang, X.; Fang, Y.; Wang, A.; Shen, H.; Du, Z., High performance blue quantum light-emitting diodes by attaching diffraction wrinkle patterns. *Nanoscale* **2021,** *13* (18), 8498-8505.

76. Bae, H. J.; Bae, S.; Park, C.; Han, S.; Kim, J.; Kim, L. N.; Kim, K.; Song, S. H.; Park, W.; Kwon, S., Biomimetic Microfingerprints for Anti-Counterfeiting Strategies. *Advanced Materials* **2015,** *27* (12), 2083-2089.

77. Zhou, Q.; Park, J. G.; Bae, J.; Ha, D.; Park, J.; Song, K.; Kim, T., Multimodal and covert–overt convertible structural coloration transformed by mechanical stress. *Advanced Materials* **2020,** *32* (25), 2001467.

78. Hou, H.; Hu, K.; Lin, H.; Forth, J.; Zhang, W.; Russell, T. P.; Yin, J.; Jiang, X., Reversible surface patterning by dynamic crosslink gradients: controlling buckling in 2D. *Advanced Materials* **2018,** *30* (36), 1803463.

79. Kim, K.; Kim, S. U.; Choi, S.; Heo, K.; Ahn, S. k.; Na, J. H., High-Definition Optophysical Image Construction Using Mosaics of Pixelated Wrinkles. *Advanced Science* **2020,** *7* (24), 2002134.

80. Wang, J.; Li, B.; Cao, Y.-P.; Feng, X.-Q.; Gao, H., Wrinkling micropatterns regulated by a hard skin layer with a periodic stiffness distribution on a soft material. *Applied Physics Letters* **2016,** *108* (2), 021903.

81. Qi, L.; Ruck, C.; Spychalski, G.; King, B.; Wu, B.; Zhao, Y., Writing wrinkles on poly (dimethylsiloxane)(PDMS) by surface oxidation with a CO2 laser engraver. *ACS applied materials & interfaces* **2018,** *10* (4), 4295-4304.

82. Schedl, A. E.; Neuber, C.; Fery, A.; Schmidt, H.-W., Controlled wrinkling of gradient metal films. *Langmuir* **2018,** *34* (47), 14249-14253.

83. Lim, J.; Choi, S. J.; Kim, P., Controlling Wrinkle Propagation in the Bilayer System with Thickness-Gradient. *Advanced Materials Interfaces* **2018,** *5* (2), 1701109.

84. Meng, Y.; Gong, X.; Huang, Y.; Li, L., Mechanically tunable opacity effect in transparent bilayer film: Accurate interpretation and rational applications. *Applied Materials Today* **2019,** *16*, 474-481.

85. Li, L.; Lin, H.; Qiao, S.; Zou, Y.; Danto, S.; Richardson, K.; Musgraves, J. D.; Lu, N.; Hu, J., Integrated flexible chalcogenide glass photonic devices. *Nature Photonics* **2014,** *8* (8), 643-649.

86. Liu, Z.; Wang, H.; Huang, P.; Huang, J.; Zhang, Y.; Wang, Y.; Yu, M.; Chen,

S.; Qi, D.; Wang, T.; Jiang, Y.; Chen, G.; Hu, G.; Li, W.; Yu, J.; Luo, Y.; Loh, X. J.; Liedberg, B.; Li, G.; Chen, X., Highly Stable and Stretchable Conductive Films through-Thermal-Radiation-Assisted Metal Encapsulation. *Advanced Materials* **2019**, 1901360.

87. Jiang, B.; Liu, L.; Gao, Z.; Wang, W., A General and Robust Strategy for Fabricating Mechanoresponsive Surface Wrinkles with Dynamic Switchable Transmittance. *Advanced Optical Materials* **2018,** *6* (13), 1800195.

88. Kumar, H. N.; Prabhakar, M.; Prasad, C. V.; Rao, K. M.; Reddy, T. A. K.; Rao, K. C.; Subha, M., Compatibility studies of chitosan/PVA blend in 2% aqueous acetic acid solution at 30 C. *Carbohydrate Polymers* **2010,** *82* (2), 251-255.

89. Groever, B.; Heshmat, B.; Raskar, R., Tyndall windows: tunable scattering of disordered solid–liquid matching mixtures. *ACS Photonics* **2016,** *3* (6), 930-935.

90. El Miri, N.; Abdelouahdi, K.; Zahouily, M.; Fihri, A.; Barakat, A.; Solhy, A.; El Achaby, M., Bio-nanocomposite films based on cellulose nanocrystals filled polyvinyl alcohol/chitosan polymer blend. *Journal of Applied Polymer Science* **2015,** *132* (22).

91. Kim, Y. H.; Jeong, H. S.; Kim, J. H.; Yoon, E. K.; Yoon, D. K.; Jung, H.-T., Fabrication of two-dimensional dimple and conical microlens arrays from a highly periodic toroidal-shaped liquid crystal defect array. *Journal of Materials Chemistry* **2010,** *20* (31), 6557-6561.

92. Knapp, A.; Nebel, L. J.; Nitschke, M.; Sander, O.; Fery, A., Controlling line defects in wrinkling: a pathway towards hierarchical wrinkling structures. *Soft Matter* **2021,** *17* (21), 5384-5392.

Acknowledgements

First of all, I am extremely grateful to Prof. Taesung Kim for his unwavering support and guidance during my Ph.D. From the moment of my Ph.D beginning, through his unconditional patience and constant inspiration, he not only guided me on the path to becoming an independent researcher, but also helped me grow as a person. Once again, I sincerely appreciate your support and guidance.

Also, I appreciate to the committee members of my dissertation, Prof. Hoon-Eui Jeong, Prof. Im Doo Jeong, at UNIST, Prof. Jungyul Park at Sogang University and Prof. Jungchul Lee at KAIST for allowing their valuable time and knowledgeable comments. I would like to give my appreciation to the members of our lab, microfluidics and nanomechatronics (uFNM) lab at UNIST. Firstly, my former lab members, Prof. Qitao Zhou. Prof. Ashish Kumar Thokchom, Dr Ronghui Wu. Dr, Qi Dong, Dr. Ji-won Lim Dr. Dogyeong ha, Dr. Jong Wan lee, Dr. Kyunghun lee, Dr. Juyeol Bae, Janghyun Ju, Youngchul Chae, Yeonghun Jeong, Dongjun Kim for valuable conversation for research and life. Also I deeply grateful for current lab member Dr. Kaliannan Thiyagarajan, Sangjin Seo, Dongwoo Seo, Hwisu Jeon, Sungjun ji for sincere support without any hesitation. I deeply wish for our lab members' bright future. Lastly I deeply grateful to my family, Jong-il Park, Inae Yang, Hyunpil Park for their dedication and effort during my Ph.D.